Contrasting Responses of Hailstorms to Anthropogenic Climate Change in Different Synoptic Weather Systems

Jiwen Fan[1,*], Yuwei Zhang[1], Jingyu Wang[1,2], Jong-Hoon Jeong[1,3], Xiaodong Chen[1], Shixuan Zhang[1], Yun Lin[1,3], Zhe Feng[1], Rebecca Adams-Selin[4]

[1] Atmospheric Science and Global Change Division, Pacific Northwest National Laboratory, Richland, Washington, USA.

[2] National Institute of Education, Nanyang Technological University, Singapore.

[3] Joint Institute for Regional Earth System Science and Engineering, University of California Los Angeles, California, USA.

[4] Verisk Atmospheric and Environmental Research, Lexington, Massachusetts, USA

* Corresponding author: Jiwen Fan

Email: *jiwen.fan@pnnl.gov*

Key points:

- Synoptic-scale environments regulate the response of hail and precipitation to anthropogenic climate change (ACC)
- The occurrence of large hail is sensitive to ACC in the frontal storms while they are not in the GPLLJ storms.
- Enhanced trough and a small increase in warm cloud depth in the future climate explain the large impact on frontal systems

This article has been accepted for publication and undergone full peer review but has not been through the copyediting, typesetting, pagination and proofreading process, which may lead to differences between this version and the Version of Record. Please cite this article as doi: 10.1029/2022EF002768.

Abstract

Hailstones and extreme precipitation generate substantial economic losses across the United States (US) and the globe. Their strong association with short-lived, intense convective storms poses a great challenge to predict their future changes. Here we conducted model simulations at 1.2 km grid spacing for severe convective storms with large hail and heavy precipitation that occurred in two typical types of synoptic-scale environments in spring seasons over the central US under both current and future climate conditions. We find that the responses of large hail (diameters > 2.5 cm) to anthropogenic climate change (ACC) are markedly different between the two types of synoptic-scale environments, with over 110% increase in large hail occurrences for the frontal systems, whereas less than 30% increase for the Great Plains low-level jet (GPLLJ) systems. This is explained by the larger increase in convective intensity and updraft width and a smaller increase in warm cloud depth in the frontal storms compared with the GPLLJ storms. Interestingly, the occurrences and intensity of heavy precipitation (rain rate > 20 mm h^{-1}) in both types of systems are similarly sensitive to ACC (e.g., 40% and 33% increases in the occurrences for the frontal and GPLLJ systems, respectively). These results might have important implications for predicting and managing risks for future hail and flash floods.

Plain Language Summary

Severe convective storms (SCSs) and associated weather hazards have caused significant property damage and economic losses worldwide. In a warming climate, how storms that presently produce hazardous weather will change and how anthropogenic warming will affect particular hazard types (for example, hail) remain highly uncertain. Through high-resolution (1.2 km grid spacing) simulations of hailstorms in spring over the central United States in both

current and future climate, we show that the hailstorms developed in the two typical types of synoptic environments have a contrasting response to climate warming. The hailstorms developed in the frontal environment are sensitive to future warming and produce much more occurrences of large hail, whereas those developed in the GPLLJ environment are not sensitive to climate warming. This study presents an important concept to study and understand the impacts of climate warming on hailstorms based on the synoptic weather systems for a specific region.

1 Introduction

Severe convective storms (SCSs) and associated weather hazards (e.g., hail, tornado, flash flood, straight wind) have caused significant property damage and economic losses worldwide (i.e., Allen, 2018 , Punge and Kunz, 2016; Guan et al., 2015). In the United States, the economic losses due to SCSs from 2007 to 2016 were $125 billion, more than all other natural hazards (i.e., droughts, flooding, and tropical cyclones) combined (Baggett et al., 2018). The impact of climate change on extreme weather events and their associated risks to the environment and society have become a pressing issue for humanity. As greenhouse gas emissions continue to rise due to human activities, the number of days with environmental conditions favoring SCSs is expected to increase (Trapp et al., 2007; Brooks, 2013; Diffenbaugh et al., 2013; Allen, 2018). However, how storms that presently produce weather hazards will change in a future warmer world and how anthropogenic warming will affect particular hazard types (for example, hail or tornadoes) remain highly uncertain (Brooks, 2013; Brimelow et al., 2017; Allen et al., 2020; Raupach et al., 2021). Although downscaling simulations at convection-permitting scales showed an increased frequency of large hail in a warming climate (Mahoney et al., 2012; Raupach et al., 2021), the level of understanding and confidence in how SCSs, including hailstorms, will be affected by anthropogenic climate change (ACC) is the lowest among all extreme events (NASEM, 2016; Brimelow et al., 2017; Allen et al., 2020).

A primary challenge to address the response of SCSs and their attendant hazards to ACC is their fine spatial scales that fall well below the effective resolution of typical global climate models (GCMs) (Trapp and Hoogewind, 2016). Hazard events such as hail and extreme rainfall occur on a spatial coverage of several to tens kilometers and a temporal scale of minutes to hours, much smaller than the features the current GCMs can generally capture. Therefore, prior

efforts toward addressing ACC effects on SCSs focused on the environmental parameters that characterize the potential for developing SCSs, e.g., convective available potential energy (CAPE) and vertical wind shear 0–6 km (S06). Those studies found that S06 generally decreases, and the CAPE largely increases over most future time periods (Diffenbaugh et al., 2013; Trapp et al., 2017). Because of significant weaknesses associated with the environmental proxy approach (Prein et al., 2015), convective-permitting models (CPMs; 4-km grid spacing or smaller) are necessary to explicitly simulate storms and provide a more robust assessment of their future changes. Due to limitations of either models or computational power in running GCMs at CPM scales, the dynamical downscaling (Trapp et al., 2011; Gensini and Mote, 2015) and the pseudo-global warming (PGW) methodology (Schär et al., 1996) were applied to fill in this gap over a region of interest. PGW has been widely used in studies associated with climate change impacts on deep convective storms and associated hazards (Rasmussen et al., 2011; Lackmann, 2013; Prein et al., 2017). Recent work showed the suitability of the PGW approach as it demonstrated the full climate change signal from a GCM-driven simulation (Kröner et al., 2017). Future projections on the convective scale showed that the frequency of large hail (> 2 cm) increases (Trapp et al., 2019; Leslie et al., 2008). However, other studies showed reduced hail frequency, particularly for small hail due to the increased melting level (Mahoney et al., 2012; Brimelow et al., 2017; Prein and Heymsfield, 2020).

Hail formation and growth processes are very complicated. Large convective instability, atmospheric humidity, and vertical wind shear can favor the development of intense hailstorms (e.g., Foote, 1984; Ilotoviz et al., 2016 ; Allen et al., 2020). Stronger updraft speeds and increased updraft width in-cloud, as well as more supercooled droplets, enhance hail formation and growth (Ziegler et al., 1983; Foote, 1984; Adams-Selin and Ziegler, 2016; Khain et al.,

2011; Lin et al., 2021). Because overly strong updrafts may eject hail out of the optimal growth region too fast (Adams-Selin and Ziegler, 2016), increasing amounts of instability only aid hailstone growth up to a point, after which it results in reduced hail sizes (Lin and Kumjian, 2022). Wider updrafts allow hail embryos to remain in updrafts longer and experience more growth (Nelson, 1983; Foote, 1984); shear profiles with increased deep-layer shear, particularly in the zonal direction, aid in the creation of wide updrafts and increased hailstone residence time (Kumjian and Lombardo, 2020). A larger amount of supercooled liquid which increases accretion riming is favorable for hail growth (Foote, 1984; Khain et al., 2011; Lin et al., 2021). The supercooled liquid can be modulated by the warm cloud depth (WCD), defined as the vertical distance between the cloud base and the melting level height. A deeper WCD leads to stronger warm rain because of enhanced collision-coalescence, reducing the amount of cloud liquid reaching the mixed-phase layer (Narsey et al., 2019; Prein et al., 2020).

Given the microscale processes involved in hail growth, it is unsurprising that previous ACC studies have uncovered conflicting signals in the response of hailstorms to ACC. Also, for different regions, hailstorm environments vary, which poses great challenges for modeling the present hail frequency and anticipating the response of hail to climate change (Zhou et al. 2021). Here we will explore these signals through the framework of differing synoptic regimes which are better understood and more predictable than hail, so the underlying environmental ingredients are varied in concert in a physically realistic manner. The study region is the central US because of the highest occurrences of hail in the United States (Cintineo et al., 2012). While previous severe weather taxonomies in the literature are numerous for this region, they have generally focused on tornadoes (e.g., Brooks et al., 1994; Garner, 2013; Anderson-Frey et al., 2017) or flash flooding/Mesoscale Convective Systems (e.g., Maddox, 1983; Yang et al., 2017;

Song et al., 2019). We turn to a general warm-season precipitation regime taxonomy in Wang et al. (2019). Over the Great Plains during spring seasons storms are mainly associated with two types of synoptic-scale environments: the frontal systems featured with a strong middle-level trough (Maddox, 1983) and strong wind shear and the Great Plains low-level jet (GPLLJ) characterized by broad and deep (extending to Northern Great Plains) low-level moisture transport (Wang et al., 2019). They correspond to Classes 1A and 1B, respectively, in Wang et al. (2019). For GPLLJs, the enhancement of the low-level jet may come from the strong North Atlantic Subtropical High system which increases the pressure gradient to help create a strong jet (Wei et al., 2019). This leads to the interesting science questions that we address in this study: (1) how do typical hailstorms and their attendant hazards over the Great Plains respond to ACC and (2) do the ACC impacts between the two major types of hailstorms differ? Answering these questions not only increases our confidence in understanding the impacts of climate change on SCSs but also improves our knowledge of hazard predictability by linking hazards with the large- and synoptic-scale environments that are better predicted by GCMs.

Here we conduct model simulations using the Weather and Research Forecast (WRF) model (Skamarock and Klemp, 2008) at 1.2 km grid spacing to simulate eight present-day hailstorms with four for each synoptical type (i.e., the frontal and GPLLJ types). The frequency of observed hail in central US peaks in the springs, April-June (Jeong et al., 2020; 2021), thus the cases are carefully selected from April-June of 2015-2017. We explore how those hailstorms would change by 2050 under the business-as-usual (high-end) emission scenario (RCP8.5) by

using the PGW approach to run the simulations in the future climate and comparing them with the simulations in the current climate.

2 Methods

2.1 Case selection and description

We carefully selected eight cases from the spring of 2015-2017, with four occurring in the frontal environment (cases 1-4) and four in the GPLLJ environment (cases 5-8; Table 1 and Figure 1). Based on SPC reports and NEXRAD we first identified hailstorm cases with hail reports larger than 100 from the spring seasons of 2015-2017. Then we examined the North American Regional Reanalysis (NARR) data for the synoptical-scale environment of each identified case. As described in the literature (Wang et al., 2019, Yang et al., 2017; Song et al., 2019), the frontal environment is featured with a low pressure rendering a strong middle-level trough and convective initiation occurring in the warm sector of the front line, whereas the GPLLJ environment has distinct features of a large subtropical ridge dominating the eastern US and a strong southerly transport of moisture from the Gulf to the region where the storm occurs. With these criteria, we obtained 6 or more hailstorm cases for each type. These cases were further filtered by model evaluation since some cases cannot be captured by the model. Eventually, four cases were obtained for the front and GPLLJ environments, respectively, with 500 hPa geopotential height and wind and 850 hPa specific humidity and wind shown in Figure 1. There are situations where convection was not initiated by the front or low-level jet and both could exert influence. We excluded those cases from this study. The radar reflectivity and hail reports of each storm are shown in Figures S1, S2, S3, and S4. A brief description is given below for each case.

Cases 1-4 formed in the typical frontal environment over the Great Plains. In case 1, a trough of low pressure created a lift along the Rio Grande Plains (Figure 1a). The low-pressure system situated over the Rocky Mountains and the upper-level jet led to a large mesoscale squall-line system (Figure S1). Widespread severe hail and a few isolated significant severe hails were reported (Figure S3). From the mesoscale perspective (Figure S5), there was a surface stationary front in the northwest of the study domain, which facilitated the convection initiation at the southeast of the low-pressure center. For case 2, a cold front over the northwestern US extended southwestward to a surface low-pressure center over northwestern Kansas (Figure 1), where a strong surface trough formed (Figure S5), and later severe thunderstorms were initiated producing large hail (Figures S1 and S3). The simulated storm is the sagging flank of the cold front where the majority of hail events occurred. Case 3 formed when the low-pressure system continued pushing to the east and a near-surface boundary front was formed across southern and central Texas in the warm sector of the cold front (Figures 1 and S5). This boundary separated moist air ahead of it and the dry air behind it. It helped lift the air to produce the convective storm across areas of eastern Texas (Figure S1). This case also featured widespread large hail (Figure S3). In case 4, a surface cold front extended from the front range of Colorado eastward into west-central Kansas (Figure S5). Cumulus clouds developed across eastern Colorado into northwestern Kansas along with the large-scale ascent associated with the upper low-pressure center over the central Plains (Figure S1), producing large hail (Figure S3).

Cases 5-8 formed in the GPLLJ environment with a strong high-pressure system (Figure 1b). Compared with the frontal systems, the low-level moisture transport in GPLLJ is much stronger and extends much further into the north. In case 5, a broad upper-level trough accompanied by a strong LLJ was evident west of the North Atlantic Subtropical High (NASH).

Correspondingly, a stationary front and a warm front formed, respectively, in the west and north of the study domain (Figure S6). The convective cells formed and organized through the strengthening of cold pools, leading to a well-organized and eastward-propagating MCS (Figure S2) and producing severe hail at the boundaries of Oklahoma and Arkansas and of Texas and Louisiana (Figure S4). In case 6, supercell structures formed over the intersection of the surface boundary and the dryline on the mesoscale (Figure S6), evolving into a large cluster of severe thunderstorms with an embedded supercell producing plenty of severe hail (Figure S2). In case 7, convective storm clusters formed aligned with the large-scale cold front, exhibiting a linear presentation but the embedded convective cores are not connected so it is not a squall line (Figure S2). Strong surface southwesterly winds overlaid with GPLLJ facilitated the updraft rotation, which favored the production of severe hail (Figure S4). In case 8, cumulus clouds immediately developed to the east of a well-defined dryline over the Texas Panhandle and South Plains, which later evolved into a supercell across Texas and produced ample severe and significant severe hail (Figures S2 and S4).

Overall, these cases cover different storm modes, namely squall lines (cases 1, 2, and 5), supercells (cases 6 and 8), multicells (cases 3 and 7), and scattered thunderstorms (case 4).

The local environment prior to storm initiation in the frontal systems is similarly warm near the surface as the GPLLJ systems (black line in Figure 2), suggesting that the convective storms of the frontal systems are hatched within the warm sector ahead of the low-pressure center. Compared with the frontal systems (Figure 2a), the GPLLJ environment (Figure 2b) features much higher precipitable water (a mean of 27.3 of GPLLJ vs. 17.5 kg m^{-2} of the front systems), CAPE (2212 vs.1130 J kg^{-1}), and storm-relative helicity (SRH; 166 vs. 101 m^2 s^{-2}), and weaker deep wind

shear between 0-6 km (S06; 14.4 vs. 16.5 m s^{-1}). GPLLJ-type storms are stronger based on CAPE and radar reflectivity, and more hail-productive compared with frontal-type storms.

2.2 Model simulations

We performed hailstorm simulations for the current and future climate with the WRF v3.9.1 model at 1.2-km grid spacing, meaning that deep convective storms are explicitly resolved, instead of parametrized with cumulus parameterizations at coarse resolutions. The model domain for the simulations covers the central United States (i.e., the plotted domain in Figure S1). The model domain includes 1,500×1,550 grid points and 65 stretched vertical levels topped at 50 hPa. We employed the NSSL two-moment microphysics scheme (Mansell et al., 2010; Mansell and Ziegler, 2013). The NSSL scheme is more advanced than many other two-moment schemes since it predicts droplet number concentrations and calculates droplet diffusional growth by allowing supersaturation (not the saturation adjustment approach). The scheme also separates rimed-ice particles into graupel and hail. The graupel category includes small hail (< 4 mm) in its size and density spectrum, whereas the hail category is designed to simulate larger hail sizes produced by wet growth of large graupel. The other model physics paramet erizations include the Noah land surface scheme, the planetary boundary layer scheme from Mellor-Yamada-Janjić, and the rapid radiative transfer model for general circulation model (RRTMG) longwave and shortwave radiation schemes.

The initial and boundary conditions for the current atmospheric state variables are from the Rapid Refresh (RAP) analysis data at 13-km grid spacing and 6-h temporal intervals (Benjamin et al., 2016). The modeled dynamic time step is 4 s, and simulations for each case

integrate over 2 days with 6 hours for spin-up. The simulation output frequency used for the analysis is 30-min. The major storm period for each case is shown in Table 1.

The simulations for the future climate were performed with the PGW approach. This methodology consists of adding a climate perturbation signal to a contemporary high-resolution reanalysis of the atmosphere during the future period of interest. For the climate perturbation signal, we subtracted the current (2009–2018) monthly 10-yr climatology from the middle century (2045–2055) monthly 10-yr climatology using the Geophysical Fluid Dynamics Laboratory Climate Model version 3 (GFDL CM3) simulation under the RCP 8.5, which is from the phase 5 of the Coupled Model Intercomparison Project (CMIP5). The reason for choosing the use of GFDL CM3 is that past studies have demonstrated GFDL CM3 to be a high-performing GCM in terms of its ability to represent the historical climatology of convective parameters and severe weather environments as compared to both reanalysis and radiosonde observations (Baggett et al., 2018; Seeleyand Romps, 2015), and it was used by a few recent studies (Trapp et al., 2019; Hoogewind et al., 2017). The climate perturbation fields include temperature, water vapor mixing ratio, geopotential height, wind, and soil moisture. The data were processed every 6-hour, so the climate change signal of the diurnal cycle was taken into account. They were interpolated and added to the corresponding fields in the RAP data and the WRF simulations for the future climate were driven by the climate-perturbed RAP data.

2.3 Convective system tracking

Since the model domain is large and often has multiple storms occurring in different places, the targeted hailstorm coverage and propagation need to be identified so that the hail and precipitation associated with the storm can be extracted and accurately accounted for. Thus, convective system tracking was applied in this study. The algorithm for tracking convective

storms was modified based on the original Flexible Object Tracker (FLEXRTKR) algorithm. FLEXRTKR was originally designed for the tracking of MCSs (Feng et al., 2018) but it was recently updated to track convective cells using radar observations (Feng et al., 2022). Here, we first identify convective systems using the composite (column maximum) radar reflectivity of 10 dBZ or larger and the contiguous area of such reflectivity exceeding 400 km^2. Then the FLEXRTKR examines the area overlap of convective systems between two adjacent time steps (a 30 min interval). If the two overlapping convective systems exceed 30% of their area, they are determined to be the same system and proceed to the next time step. The tracked system terminates when the overlapping threshold is no longer met. This convective system tracking allows us to track individual convective cells producing hail such as supercells as well as those that grow and aggregate upscale to MCSs.

2.4 Data and data analysis

Two independent hail observational datasets were used for model evaluation: the hail reports and radar-retrieved maximum expected size of hail (MESH). The hail reports were obtained from the National Oceanic and Atmospheric Administration (NOAA) Storm Prediction Center (SPC) Warning Coordination Meteorologist page (https://www.spc.noaa.gov/wcm/). The MESH data used in this study were developed with a newly improved algorithm, which had better agreements with hail reports by using the revised the power-law relationship and refitted 95th percentile of observed hail size (Murillo and Homeyer, 2019). The new MESH data with the 95th percentile fit was also used in the recent studies for examining the hail interannual variability over the Great Plains (Jeong et al., 2020; 2021). The observed precipitation data is from the National Centers for Environmental Prediction (NCEP) stage-IV data (Du, 2011) that

provides hourly precipitation estimates at 4-km horizontal grid spacing based on radar and surface rain gauges.

In the model simulations, the maximum hail size at the ground is diagnosed from the predicted hail size distribution N(D) represented by a gamma distribution function in NSSL. There are two approaches employed in the literature: the Thompson approach which integrates over N(D) from the large size end until the number reaches a threshold (Milbrandt and Yau, 2006; Thompson et al., 2018) and the Snook approach (Snook et al., 2016) which intercepts N(D) at 10^{-4} m^{-3} mm^{-1}. For the former, different thresholds were used in the literature such as 1×10^{-4} used in Milbrandt and Yau (2006) and 5×10^{-4} m^{-3} used in WRF v4.0. We tested both approaches with the different thresholds and found a Thompson approach with the threshold of 10^{-5} m^{-3} overall gives the best results compared against hail reports and MESH. Therefore, this approach was employed for the maximum hail size calculation. The conclusions about how ACC impacts hail occurrences for both types of systems are not influenced by the different methods and thresholds used (see the discussion in the last section).

The analysis of updraft velocity and hydrometeors is for grids with vertical velocity (w) larger than 5 m s^{-1} at each vertical level. The updraft width is represented by the number of horizontally adjacent updraft grids with $w > 5$ m s^{-1} at each level. For example, the updraft width of 8 means that 8 updraft grids with $w > 5$ m s^{-1} are connected. We used the standard deviation to represent the uncertainty. For updraft velocity, we tried different ways (e.g., the percentile) or threshold (e.g., $w > 3$ m s^{-1}) to process the data. The conclusions are all consistent.

3 Results

3.1 Evaluation of present-day storms

We first evaluated the model simulations in the current climate with observed reflectivity, hail, and precipitation (Figures 3, S1-S4). The simulated frequency distributions of reflectivity, precipitation, and hail are consistent with observations in general for both the frontal and GPLLJ storms (Figure 3), despite the model tending to overestimate frequencies of large radar reflectivity and rain rates. From the snapshot plots of reflectivity for each storm (Figures S1-S2), the overall morphology and organization are well simulated, except for an overestimation in reflectivity. Large overestimation of reflectivity has been commonly found in WRF simulations (Gallus and Pfeifer, 2008; Molthan et al., 2016; Varga and Breuer, 2020). For each case, the hail swath is captured well (Figures S3-S4). For hail frequencies, it is difficult to judge the model performance since the MESH data predicted over 100 times higher occurrences of large hail than the hail reports (Jeong et al., 2020; 2021), which seems too high, whereas the hail reports suffer from low biases, due to non-meteorological factors such as the remote area and nighttime period. The hail reports from SPC plotted in Figures S3-S4 include data one hour before and after the study time to account for the uncertainty of hail reports. This calls for more robust observation data for hail to evaluate model performances.

3.2 Hail and precipitation changes from the current to future climate

From the current to future climate, the storms developed in the frontal environment exhibit markedly increases in the occurrence of large hail in the future climate with a mean increase of ~ 114% for severe hail and ~ 145% for significant severe hail (Figure 4a-b). In contrast, the GPLLJ cases have very small increases in the hail frequencies (28% for severe hail and ~ 18% for significant severe hail). When looking at the changes in hail frequency from the current to future climate case by case (Figure S7), we can see all four cases of the frontal type

have large increases in all sizes and overall, the increase is larger as the size increase (over 100% generally for a size larger than 3.5 cm, whereas all GPLLJ cases have small changes (less than 50% generally). We see that the GPLLJ storms produce an order of magnitude more severe and significant severe hail than the frontal storms in the current climate (Figures 4a and S7). Therefore, large hail in the frontal storms is more sensitive to the ACC compared with that in the GPLLJ storms, with much larger increases in frequencies of large hail in the frontal storms.

For precipitation, there is a 40% and 45% increase in the heavy rain (> 20 mm h^{-1}) frequency and amount, respectively, for the frontal storms, and the corresponding values for GPLLJ storms are 33% and 38% (Figures 4c-f). Therefore, the responses to ACC are of a similar magnitude between the two types of storms. It is worth noting is that the response in the frequency and amount of weak rain (0.1 mm h^{-1} < rain rate ≤ 5 mm h^{-1}) is reduced for the frontal storms (-17% in frequency and -12% in amount) but there is a small increase for the GPLLJ storms (14% in frequency and 10% in amount). The moderate rain (5 mm h^{-1} < rain rate ≤ 20 mm h^{-1}) increases in a similar magnitude as the light rain for the GPLLJ storms but does not change much for the frontal storms.

3.3 Changes in meteorological environments

On the synoptic scale, from the current to future climate, the geopotential height at 500 hPa and near the surface increases in all cases (Figure 1a vs. S8a). For the frontal systems, although the geopotential height of the low-pressure center becomes higher, the horizontal gradient on the trough near the convective initiation region becomes stronger (the gradient increase by 5.2% from current to future climate). In the GPLLJ cases, the change of horizontal gradient on the ridge of the high-pressure system is not as much as those of frontal systems (less than 3.8%), but the high-

pressure system pushes more northwardly leading to a stronger transport of moisture in the central US (Figure 1b vs. S8b). The increases in temperature in the GPLLJs are larger than in the frontal systems across the vertical profile, particularly near the surface (Figure S9). The larger increase in temperature in the GPLLJs could favor more melting but Xie et al. (2010) showed that melting has a negligible effect on the size of large hail. The larger increase in temperature in the GPLLJs may contribute to a smaller increase in RH below 2 km than the frontal systems. The surface wind pattern is not changed much in general.

On the mesoscale, in the frontal systems, the change from the current to future climate makes the environment more favorable for the initiation of stronger convection (Figure S5). In cases 1, 3, and 4, the temperature contrast is greatly intensified along the surface front, mainly because the future warming is more prominent on the warm side, which is located southeast of the study domain. For case 2, the surface trough grows deeper in the future climate compared to the current climate. In contrast, the mesoscale environment in the GPLLJs (Figure S6) is either unchanged (cases 7 and 8) or slightly weakened (cases 5 and 6) for convection initiation. In cases 5 and 6, the stationary front is north-south oriented, and the future warming increases the near-surface temperature on the east side (also the relatively cold side) of the fronts, which mitigates the temperature gradient and subsequently results in weaker fronts. In cases 7 and 8, although the surface fronts are also northeast-southwest oriented, the temperature increase brought by future warming has a similar effect on both sides of the fronts, leaving the temperature gradient unchanged. We do not see apparent changes in the storm modes by ACC for both types of systems (Figures S1-S2).

For the meteorological variables right before convection, the frequency distributions show that the frontal cases have a smaller shift to high values than the GPLLJ cases in 2-m

temperature (a mean increase of 0.8 in frontal systems vs. 1.8 °C in the GPLLJs) and CAPE 169.9 vs. 278.8 J kg^{-1}) from current to future climate (Figure 2). This may indicate that GPLLJ storms can be more sensitive to ACC and become stronger than frontal storms. However, the environment for the frontal storms has larger increases in CIN (a mean increase of 4.9 J kg^{-1} in frontal systems vs. 3.1 J kg^{-1} in the GPLLJs) and S06 (0.7 vs. 0.5 m s^{-1}) than that for the GPLLJ storms. This may indicate that ACC would lead to more severe storms in the frontal type than the GPLLJ type, opposite to the inference based on the 2-m temperature and CAPE. The smaller 2-m temperature and CAPE increase by ACC in the frontal systems is probably because they are located at higher latitudes than the GPLLJs so has less surface warming, and the larger increase in S06 and CIN should be related to stronger surface front and deeper trough in the future climate as described above. The precipitable water is increased similarly for both storm types in absolute differences. However, the relative increase is 19% for the frontal systems and 14% for the GPLLJs. Although the SRH has a smaller absolute increase in frontal systems than in the GPLLJs (7 m^2 s^{-2} vs. 11.9 m^2 s^{-2}), the relative increase is similar (both are ~7%).

Overall, based on the changes in the meteorological environment from the current to the future climate we have not yet gotten a clear understanding of why frontal storms are more sensitive to ACC than the GPLLJ storms.

3.4 Changes in cloud dynamics and WCD explain different sensitivities

Interestingly, the cloud dynamics in the two types of systems respond very differently to ACC. The convective intensity (denoted by updraft velocity) of the tracked frontal storms notably increases (e.g., the mean increase over 5-10 km altitudes is 6-7%) from the current to the future climate (1st panel in Figure 5a), but the change is negligible for the GPLLJ storms (1st

panel in Figure 5b). This is further corroborated by the frequency distribution of updraft velocities (Figure S10) showing enhancements in the frequencies of large updraft velocities (> 15 m s^{-1}) below 10 km altitude in the frontal storms. Whereas the GPLLJ storms show some small increases as well as small decreases. Each frontal storm shows a similar change to the composite of the four cases in both Figures 5 and S10. For the GPLLJ storms, the changes in all four cases are not large, with a small decrease for cases 5, 6, and 7 and a small increase for cases 8.

Besides the increased updraft intensity, the updraft width (i.e., the size of the updrafts; 2nd panel of Figure 5a) in the frontal storms is ~15% larger in the future climate at the mixed-phase regimes where hail forms and grows (5-10 km altitudes), which allows hail experiencing more growth to form larger hail (Ziegler et al., 1983; Foote, 1984). However, the updraft width in the GPLLJ storms is only marginally changed by ACC at 5-10 km altitudes (~ 4% between 5-10 km; 2nd panel of Figure 5b).

Correspondingly, we see large increases occurring in graupel and hail mass mixing ratios as well as the bulk hail size in those updrafts for the frontal storms (the last three columns of Figure 5), with 20-40% in graupel mass, ~60% in hail mass, and up to 8% in bulk hail size at 5-10 km altitudes. For the GPLLJ storms, the graupel and hail mass mixing ratios also increase but to a much lesser extent (~10% in graupel mass and ~30% in hail mass). Hail size does not change much since both updraft speed and width are not noticeably enhanced. A larger increase in updraft speed in the frontal storms results in more condensation and vertical transport of droplets from the lower levels, contributing to larger increases in the supercooled droplet mass compared with the GPLLJ storms (first column in Figure 6). In particular, the cloud droplet mass flux across the melting level is increased much more than in the GPLLJ storms (3rd column in

Figure 6). The larger cloud droplet mass flux crossing the melting level in the frontal system can also be contributed by the much smaller increase in WCD, which will be discussed in detail below. The presence of more supercooled droplets in the frontal storms favors riming growth for generating more graupel and hail, favoring the formation of large hail. It should be noted that there is an optimal value for updraft intensity to enhance hail frequency and size because too strong updraft speeds eject hail embryos out of the hail growth regime too quickly to allow for mature growth. As noted earlier, the frontal storms in the current climate are not that strong so the increase in updraft intensity should be favorable for hail growth. The increases in rain mass content and flux from the current to future climate are similar between the two types of storms (2nd and 4th columns in Figure 6).

To explain why the convective intensity in the frontal storms is increased by ACC while there is a limited change in the GPLLJ storms, we examined the vertical velocity components as shown in Figure 7. We find that the increase in the vertical pressure perturbation gradient (PPG) force at the lower and middle troposphere is the main factor responsible for enhanced updraft speeds in the frontal storms (~ 30% at 4 km; 1st panel in Figure 7a). All four frontal storms exhibit an increase, consistent with the updraft velocity increase in each case). However, in GPLLJ storms, the mean PPG force does not change much in the future climate (~ 5% increase; 1st panel in Figure 7b). Also consistent with the updraft velocity changes, the changes in all four cases are not large, with a small decrease for cases 5, 6, and 7 and a small increase for 8). The changes in thermal buoyancy in response to ACC are small in both types of storms. The hydrometeor loading effect increases more in the frontal storms than in the GPLLJ storms (3rd column in Figure 7) since the precipitable water and convective intensity have a larger increase. In the GPLLJ storms, the changes in every term contributing to vertical velocity change

including PPG, thermal buoyancy, hydrometeor loading, and entrainment are small (Figure 7b). The increased PPG in the frontal systems from the current to the future climate probably results from the stronger horizontal pressure gradient on the trough, whereas the small change in the horizontal pressure gradient on the ridge of the high-pressure system in the GPLLJs may be the reason for the small increase in PPG.

For the squall line system, convection initiation is sensitive to the intensity of the cold pool (i.e., Chen et al., 2015; Li et. al., 2017). We investigated the cold pool changes for the three squall line cases: Case 1 and Case 2 from the frontal group and Case 5 from the GPLLJ group. For each case, we selected a cold pool area (i.e., 50 km × 50 km) behind the leading edge of the convective system and obtained the ratio of cold pool strength (c) to the low- level wind shear strength (Δu_{max}) following the definition and calculation in Chen et. al. (2015). Based on the Rotunno- Klemp- Weisman (RKW) theory, upright cores are more favorable when $c/\Delta u_{max}$ is closer to 1. We found that the values of $c/\Delta u_{max}$ are larger than 1 for three cases and they change little from the current to future climate (i.e., 1.4 for Case 1 and no change; from 1.7 to 1.8 for Case 2; from 1.9 to 1.8 for Case 5). Therefore, the cold pool change should not be a reason for the different enhancement in convection between frontal storms and GPLLJ storms.

Although the CAPE increases more in the GPLLJs compared with the frontal systems, the convective intensity of the GPLLJ storms in the current climate is already very strong because of the large CAPE so the storm intensity is not sensitive to a further increase in CAPE. However, the frontal storms are relatively moderate in the current climate, and they become notably stronger in the warming climate. Therefore, moderate present-day storms might be sensitive to climate change, while very strong present-day storms might not.

As discussed above, the much larger increase in the supercooled droplet mass for the frontal storms from the current to future climate compared to the GPLLJ storms can be contributed by different changes in WCD by ACC between the two types of storms. This is because deeper WCD allows more droplets to form rain and fallout when updraft speeds are not changed substantially, so fewer droplets will be transported across the melting level to become supercooled droplets. Indeed, we found that the increase in WCD in the convective cores (defined in Figure 8 caption) in the frontal storms (a mean increase of 85 m) is a lot smaller than the increase in the GPLLJ storms (a mean increase of 357 m; Figure 8c). The distribution of WCD shows a larger shift to high values in GPLLJ storms compared to the frontal storms (Figure 8a-b). Therefore, shallower WCD in the frontal storms in the future climate allows more droplets to be lifted to temperatures below 0 °C and favors the riming growth of hail. It is worth noting that increased supercooled droplets can also induce stronger ice microphysical processes such as freezing and deposition, which releases more latent heat and intensifies storms (e.g., Khain et al., 2005; Fan et al., 2007; 2018).

The changes in both the melting level height and the cloud base height (CBH) from the current to future climate contributed to the small increase in WCD for the frontal storms but the large increase for the GPLLJ storms (Figure 8d-i). The mean melting level height increases by 101 m only in the frontal systems but 292 m in GPLLJs (Figure 8f). The mean CBH increases by 16 m in the frontal systems but decreases by 65 m in GPLLJs (Figure 8i). As a result, the increase in WCD in the frontal storms is limited but much larger in the GPLLJ storms. The melting level increase is positively correlated with the 2-m temperature increase (Prein and Hemysfield, 2020). The 2-m temperature increase by ACC in the frontal systems is lower than that in the GPLLJs (Figure 2) explaining the smaller increase in the melting level height. The decreased difference between the

temperature and dew temperature near the surface from the current to future GPLLJ storms results in a lower lifting condensation level (LCL) thus the decreased CBH.

4. Conclusion and discussion

Through high-resolution (1.2 km grid spacing) simulations of hailstorms in spring over the central US in both current and future climate, we find that the hailstorms developed in the two typical types of synoptic environments have a contrasting response to ACC (Figure 9). The hailstorms developed in the frontal environment are sensitive to future climate change and produce much more occurrences of severe hail (~ 114%) and significant severe hail (~ 145%) whereas those developed in the GPLLJ environment are not sensitive to ACC, with only 28% increase in the several hail and 18% increase in the significant severe hail. Interestingly, the occurrences and intensity of heavy precipitation (rain rate > 20 mm h^{-1}) from both types of systems are similarly sensitive to ACC, with a 40% and 33% increase in the occurrences for the frontal and GPLLJ systems, respectively.

The major reasons for the large increases in large hail by ACC for the frontal storms but small changes for the GPLLJ storms include (a) the enhanced updraft speeds and increased updraft width in the frontal storms whereas negligible changes in the GPLLJ storms and (b) the smaller increases of WCD in the frontal storms than in the GPLLJ storms. Both enhanced convection intensity and smaller WCD increases support more supercooled liquid, leading to stronger freezing and riming that produces more graupel and hail. The increased updraft width further enhances hail growth. The intensified convection in the frontal systems in the future climate is due to enhanced vertical pressure gradient perturbation, associated with the stronger trough. The smaller increase of WCD in the frontal storms is because (a) the melting level rise is

less significant than in the GPLLJ storms and (b) there is a slight increase in cloud base height in the frontal storms but a reduction in the GPLLJ storms.

We also showed the impact of ACC on heavy and extreme precipitation does not much depend on storm types defined by synoptic features. A possible reason for the different responses is that hail and precipitation have very different formation mechanisms in both dynamics and microphysics. Hail formation and growth are sensitive to the changes in melting level, cloud base height, and vertical pressure gradient perturbation, which tie closely to changes in the synoptic environment.

Since the maximum hail size calculation for model simulations have different methods and the threshold to truncate hail size distribution is uncertain as discussed in Section 2.4, we conducted sensitivity tests by changing the threshold used for our results from 10^{-5} m^{-3} to 5×10^{-4} m^{-3} and using a different approach- the Snook approach to see how our conclusions are impacted. It is clear that the different methods and thresholds affect the magnitude of the hail occurrences but do not affect our conclusions about ACC impacts on hail for both types of storms (Figure S11).

It is noted that our results might have uncertainties due to the following aspects. (1) For each case, we do not carry out ensemble simulations by perturbing the initial and boundary conditions or physical parameterizations due to the limitation in computing resource. Ensemble runs would describe the simulation uncertainty to some extent. (2) The changes of meteorological environment might be different between the two types of the systems occurring in the same month. Here we use the same mean monthly climate perturbation signal averaged over 10 years to get the robust climate change signal. Note the diurnal cycle of climate change signal was considered in this study which was usually not done in previous studies. (3)

Additionally, aerosols, which are also important in affecting the hail and precipitation (i.e., Li et. al., 2021), may change in the future climate. Here we focused on the climate change impact and did not consider aerosol changes, which can be a topic of future studies.

This study shows that synoptic-scale features regulate the response of storms to anthropogenic warming in the central United States. By linking the impacts of ACC on hailstorms to the dominant synoptic-scale feature that can be better predicted by global models, this study advances our knowledge of hailstorm predictability and increases our confidence in the future projection of hail. Therefore, in terms of the climate prediction of SCSs and the attendant hazards, this study presents an important concept to study and understand ACC impacts based on the synoptic scale features which are usually predictable for a specific region. As an initial study of this concept, we only examined hail-producing storms for spring in the central United States. The follow-on steps can be (a) the long-term studies for this region which is currently computationally prohibitive for us and (b) the application of the concept to the other regions to advance our understanding of climate prediction of hail region by region.

Acknowledgments

This study is supported by the U.S. Department of Energy (DOE) Office of Science Early Career Award Program 70017 (all authors). Pacific Northwest National Laboratory is operated for the U.S. Department of Energy (DOE) by Battelle Memorial Institute under contract DE-AC05-76RL01830. This research used resources of the National Energy Research Scientific Computing Center (NERSC). NERSC is a U.S. DOE Office of Science User Facility operated under Contract No. DE-AC02-05CH11231. The GFDL CM3 simulations can be accessed from https://esgf-node.llnl.gov/projects/esgf-llnl/. The reflectivity data is available at

http://gridrad.org/. Hail reports are available from the NOAA Storm Prediction Center https://www.spc.noaa.gov/archive/. The stage-IV precipitation data can be downloaded at https://data.eol.ucar.edu/dataset/21.093/. The WRF model simulation data can be accessed from https://portal.nersc.gov/project/m2977/hail_acc after the paper is accepted.

References

Adams-Selin, R. D., &Ziegler, C. L. (2016). Forecasting hail using a one-dimensional hail growth model within WRF. *Monthly Weather Review*, *144*(12), 4919-4939. doi:10.1175/Mwr-D-16-0027.1.

Allen, J. T. (2018), Climate change and severe thunderstorms, in *Oxford Research Encyclopedia of Climate Science*, edited, pp. 1-67.

Allen, J. T., Giammanco, I. M., Kumjian, M. R., Punge, H. J., Zhang, Q. H., Groenemeijer, P., Kunz, M., &Ortega, K. (2020). Understanding hail in the Earth system. *Reviews of Geophysics*, *58*(1). doi:10.1029/2019RG000665.

Anderson-Frey, A. K., Richardson, Y. P., Dean, A. R., Thompson, R. L., and Smith, B. T. (2017). Self-organizing maps for the investigation of tornadic near-storm environments. *Wea. Forecasting*, *32*, 1467–1475

Baggett, C. F., Nardi, K. M., Childs, S. J., Zito, S. N., Barnes, E. A., &Maloney, E. D. (2018). Skillful subseasonal forecasts of weekly tornado and hail activity using the Madden-Julian Oscillation. *Journal of Geophysical Research-Atmospheres*, *123*(22), 12661-12675. doi:10.1029/2018jd029059.

Benjamin, S. G., Weygandt, S. S., Brown, J. M., Hu, M., Alexander, C. R., Smirnova, T. G., Olson, J. B., James, E. P., Dowell, D. C., Grell, G. A., Lin, H. D., Peckham, S. E., Smith, T. L., Moninger, W. R., Kenyon, J. S., &Manikin, G. S. (2016). A North American hourly assimilation and model forecast cycle: The rapid refresh. *Monthly Weather Review*, *144*(4), 1669-1694. doi:10.1175/Mwr-D-15-0242.1.

Brimelow, J. C., Burrows, W. R., &Hanesiak, J. M. (2017). The changing hail threat over North America in response to anthropogenic climate change. *Nature Climate Change*, *7*(7), 516-522. doi:10.1038/Nclimate3321.

Brooks, H. E., Doswell, C. A., and Cooper, J. (1994). On the environments of tornadic and nontornadic mesocyclones. *Weather and Forecasting*, *9*, 606–618.

Brooks, H. E. (2013). Severe thunderstorms and climate change. *Atmospheric Research*, *123*, 129-138. doi:10.1016/j.atmosres.2012.04.002.

Chen, Q., Fan J., Hagos S., Gustafson Jr. W. I., & Berg L. K. (2015), Roles of windshear at different vertical

levels: Cloudsystem organization and properties, *J. Geophys. Res. Atmos*.,120, 6551–6574, doi:10.1002/2015JD023253.

Cintineo, J. L., Smith, T. M., Lakshmanan, V., Brooks, H. E., & Ortega, K. L. (2012). An objective high-resolution hail climatology of the contiguous United States. Weather and Forecasting, 27(5), 1235-1248. https://doi.org/10.1175/WAF-D-11-00151.1.

Diffenbaugh, N. S., Scherer, M., &Trapp, R. J. (2013). Robust increases in severe thunderstorm environments in response to greenhouse forcing. *Proceedings of the National Academy of Sciences of the United States of America*, *110*(41), 16361-16366. doi:10.1073/pnas.1307758110.

Du, J. (2011). NCEP/EMC 4KM Gridded Data (GRIB) Stage IV Data. Version 1.0. *UCAR/NCAR - Earth Observing Laboratory*. https://doi.org/10.5065/D6PG1QDD

Fan, J. W., Rosenfeld, D., Zhang, Y. W., Giangrande, S. E., Li, Z. Q., Machado, L. A. T., Martin, S. T., Yang, Y., Wang, J., Artaxo, P., Barbosa, H. M. J., Braga, R. C., Comstock, J. M., Feng, Z., Gao, W. H., Gomes, H. B., Mei, F., Pohlker, C., Pohlker, M. L., Poschl, U., &de Souza, R. A. F. (2018). Substantial convection and precipitation enhancements by ultrafine aerosol particles. *Science*, *359*(6374), 411-418. doi:10.1126/science.aan8461.

Fan, J. W., Zhang, R. Y., Li, G. H., &Tao, W. K. (2007). Effects of aerosols and relative humidity on cumulus clouds. *Journal of Geophysical Research-Atmospheres*, *112*(D14). doi:10.1029/2006jd008136.

Feng, Z., Leung, L. R., Houze, R. A., Hagos, S., Hardin, J., Yang, Q., Han, B., &Fan, J. W. (2018). Structure and evolution of mesoscale convective systems: Sensitivity to cloud microphysics in convection-permitting simulations over the United States. *Journal of Advances in Modeling Earth Systems*, *10*(7), 1470-1494. doi:10.1029/2018ms001305.

Feng, Z., Varble A,, Hardin J., Marquis, J., Hunzinger, A., Zhang, Z., and Thieman M. (2022). Deep Convection Initiation, Growth and Environments in the Complex Terrain of Central Argentina during CACTI, *Monthly Weather Review*, https://doi.org/10.1175/MWR-D-21-0237.1.

Foote, G. B. (1984). A study of hail growth utilizing observed storm conditions. *Journal of Climate and*

Applied Meteorology, *23*(1), 84-101. doi:10.1175/1520-0450(1984)023<0084:Asohgu>2.0.Co;2.

Gallus Jr., W. A. and Pfeifer, M. (2008). Intercomparison of simulations using 5 WRF microphysical schemes with dual-Polarization data for a German squall line. *Adv. Geosci., 16*, 109–116, https://doi.org/10.5194/adgeo-16-109-2008, 2008.

Garner, J. M. (2013). A study of synoptic-scale tornado regimes. *Electronic J. Severe Storms Meteor., 8* (3), 1–25.

Gensini, V. A., &Mote, T. L. (2015). Downscaled estimates of late 21st century severe weather from CCSM3. *Climatic Change*, *129*(1-2), 307-321. doi:10.1007/s10584-014-1320-z.

Guan, Y. H., Zheng, F. L., Zhang, P., &Qin, C. (2015). Spatial and temporal changes of meteorological disasters in China during 1950-2013. *Natural Hazards*, *75*(3), 2607-2623. doi:10.1007/s11069-014-1446-3.

Hoogewind, K. A., Baldwin, M. E., &Trapp, R. J. (2017). The impact of climate change on hazardous convective weather in the United States: Insight from high-resolution dynamical downscaling. *Journal of Climate*, *30*(24), 10081-10100. doi:10.1175/Jcli-D-16-0885.1.

Ilotoviz, E., Khain, A. P., Benmoshe, N., Phillips, V. T. J., &Ryzhkov, A. V. (2016). Effect of aerosols on freezing drops, hail, and precipitation in a midlatitude storm. *Journal of the Atmospheric Sciences*, *73*(1), 109-144. doi:10.1175/Jas-D-14-0155.1.

Jeong, J. H., Fan, J. W., &Homeyer, C. R. (2021). Spatial and temporal trends and variabilities of hailstones in the United States Northern Great Plains and their possible attributions. *Journal of Climate*, *34*(16), 6819-6840. doi:10.1175/Jcli-D-20-0245.1.

Jeong, J.-H., Fan, J., Homeyer, C. R., &Hou, Z. (2020). Understanding hailstone temporal variability and contributing factors over the United States Southern Great Plains. *Journal of Climate*, *33*(10), 3947-3966. doi:10.1175/jcli-d-19-0606.1.

Khain, A., Rosenfeld, D., &Pokrovsky, A. (2005). Aerosol impact on the dynamics and microphysics of deep convective clouds. *Quarterly Journal of the Royal Meteorological Society*, *131*(611), 2639-2663. doi:10.1256/qj.04.62.

Khain, A., Rosenfeld, D., Pokrovsky, A., Blahak, U., &Ryzhkov, A. (2011). The role of CCN in precipitation and hail in a mid-latitude storm as seen in simulations using a spectral (bin) microphysics model in a 2D dynamic frame. *Atmospheric Research*, *99*(1), 129-146. doi:10.1016/j.atmosres.2010.09.015.

Kröner, N., Kotlarski, S., Fischer, E., Lüthi, D., Zubler, E., &Schär, C. (2017). Separating climate change signals into thermodynamic, lapse-rate and circulation effects: Theory and application to the European summer climate. *Climate Dynamics*, *48*(9-10), 3425-3440. doi:10.1007/s00382-016-3276-3.

Kumjian, M. R., & Lombardo, K. (2020). A hail growth trajectory model for exploring the environmental controls on hail size: Model physics and idealized tests. *Journal of the Atmospheric Sciences*, 77(8), 2765–2791. https://doi.org/10.1175/JAS-D-20-0016.1.

Lackmann, G. M. (2013). The south-central United States Flood of may 2010: Present and future. *Journal of Climate*, *26*(13), 4688-4709. doi:10.1175/jcli-d-12-00392.1.

Leslie, L. M., Leplastrier, M., &Buckley, B. W. (2008). Estimating future trends in severe hailstorms over the Sydney Basin: A climate modelling study. *Atmospheric Research*, *87*(1), 37-51. doi:10.1016/j.atmosres.2007.06.006.

Li, M., Zhang F., Zhang Q., Harrington J. Y. & Kumjian M. R.. (2017). Nonlinear response of hail precipitation rate to environmental moisture content: A real case modeling study of an episodic midlatitude severe convective event, *J. Geophys. Res. Atmos*., 122, doi:10.1002/ 2016JD026373.

Li, X., Zhang, Q.,Fan, J.,* & Zhang, F. (2021). Notable contributions of aerosols to the predictability of hail precipitation. *Geophysical Research Letters*, 48, e2020GL091712. Doi: 10.1029/2020GL091712.

Lin, Y., Fan, J., Jeong, J.-H., Zhang, Y., Homeyer, C. R., &Wang, J. (2021). Urbanization-induced land and aerosol impacts on storm propagation and hail characteristics. *Journal of the Atmospheric Sciences*, *78*(3), 925-947. doi:10.1175/jas-d-20-0106.1.

Lin, Y., &Kumjian, M. R. (2022). Influences of CAPE on hail production in simulated supercell storms. *Journal of the Atmospheric Sciences*, *79*(1), 179-204. doi:10.1175/jas-d-21-0054.1.

Maddox, R. A. (1983). Large-scale meteorological conditions associated with midlatitude, mesoscale

convective complexes. *Monthly Weather Review*, *111*(7), 1475-1493. doi:10.1175/1520-0493(1983)111<1475:Lsmcaw>2.0.Co;2.

Mahoney, K., Alexander, M. A., Thompson, G., Barsugli, J. J., &Scott, J. D. (2012). Changes in hail and flood risk in high-resolution simulations over Colorado's mountains. *Nature Climate Change*, *2*(2), 125-131. doi:10.1038/Nclimate1344.

Mansell, E. R., &Ziegler, C. L. (2013). Aerosol effects on simulated storm electrification and precipitation in a two-moment bulk microphysics model. *Journal of the Atmospheric Sciences*, *70*(7), 2032-2050. doi:10.1175/Jas-D-12-0264.1.

Mansell, E. R., Ziegler, C. L., &Bruning, E. C. (2010). Simulated electrification of a small thunderstorm with two-moment bulk microphysics. *Journal of the Atmospheric Sciences*, *67*(1), 171-194. doi:10.1175/2009jas2965.1.

Milbrandt, J. A., &Yau, M. K. (2006). A multimoment bulk microphysics parameterization. Part iii: Control simulation of a hailstorm. *Journal of the Atmospheric Sciences*, *63*(12), 3114-3136. doi:Doi 10.1175/Jas3816.1.

Molthan AL, Colle, B.A., Yuter, S.E., Stark, D. (2016). Comparisons of Modeled and Observed Reflectivities and Fall Speeds for Snowfall of Varied Riming Degrees during Winter Storms on Long Island, New York. *Mon. Weather. Rev., 144*(11):4327-4347. doi: 10.1175/mwr-d-15-0397.1.

Murillo, E. M., &Homeyer, C. R. (2019). Severe hail fall and hailstorm detection using remote sensing observations. *Journal of Applied Meteorology and Climatology*, *58*(5), 947-970. doi:10.1175/Jamc-D-18-0247.1.

Narsey, S., Jakob, C., Singh, M. S., Bergemann, M., Louf, V., Protat, A., &Williams, C. (2019). Convective precipitation efficiency observed in the tropics. *Geophysical Research Letters*, *46*(22), 13574-13583. doi:10.1029/2019gl085031.

National Academies of Sciences, Engineering, and Medicine (NASEM) (2016). Attribution of extreme weather events in the context of climate change.(Report, pp 1-165), The National Academies Press.

Nelson, S. P. (1983). The influence of storm flow structure on hail growth. *Journal of the Atmospheric*

Sciences, *40*(8), 1965-1983. doi:10.1175/1520-0469(1983)040<1965:Tiosfs>2.0.Co;2.

Prein, A. F., &Heymsfield, A. J. (2020). Increased melting level height impacts surface precipitation phase and intensity. *Nature Climate Change*, *10*(8), 771-776. doi:10.1038/s41558-020-0825-x.

Prein, A. F., Langhans, W., Fosser, G., Ferrone, A., Ban, N., Goergen, K., Keller, M., Tolle, M., Gutjahr, O., Feser, F., Brisson, E., Kollet, S., Schmidli, J., van Lipzig, N. P. M., &Leung, R. (2015). A review on regional convection-permitting climate modeling: Demonstrations, prospects, and challenges. *Reviews of Geophysics*, *53*(2), 323-361. doi:10.1002/2014rg000475.

Prein, A. F., Liu, C. H., Ikeda, K., Trier, S. B., Rasmussen, R. M., Holland, G. J., &Clark, M. P. (2017). Increased rainfall volume from future convective storms in the US. *Nature Climate Change*, *7*(12), 880-884. doi:10.1038/s41558-017-0007-7.

Punge, H. J., &Kunz, M. (2016). Hail observations and hailstorm characteristics in Europe: A review. *Atmospheric Research*, *176*, 159-184. doi:10.1016/j.atmosres.2016.02.012.

Rasmussen, R., Liu, C. H., Ikeda, K., Gochis, D., Yates, D., Chen, F., Tewari, M., Barlage, M., Dudhia, J., Yu, W., Miller, K., Arsenault, K., Grubisic, V., Thompson, G., &Gutmann, E. (2011). High-resolution coupled climate runoff simulations of seasonal snowfall over Colorado: A process study of current and warmer climate. *Journal of Climate*, *24*(12), 3015-3048. doi:10.1175/2010jcli3985.1.

Raupach, T. H., Martius, O., Allen, J. T., Kunz, M., Lasher-Trapp, S., Mohr, S., Rasmussen, K. L., Trapp, R. J., &Zhang, Q. H. (2021). The effects of climate change on hailstorms. *Nature Reviews Earth & Environment*, *2*(3), 213-226. doi:10.1038/s43017-020-00133-9.

Schär, C., Frei, C., Lüthi, D., &Davies, H. C. (1996). Surrogate climate-change scenarios for regional climate models. *Geophysical Research Letters*, *23*(6), 669-672. doi:Doi 10.1029/96gl00265.

Seeley, J. T., &Romps, D. M. (2015). Why does tropical convective available potential energy (CAPE) increase with warming? *Geophysical Research Letters*, *42*(23), 10429-10437. doi:10.1002/2015gl066199.

Skamarock, W. C., &Klemp, J. B. (2008). A time-split nonhydrostatic atmospheric model for eather research and forecasting applications. *Journal of Computational Physics*, *227*(7), 3465-3485.

doi:10.1016/j.jcp.2007.01.037.

Snook, N., Jung, Y., Brotzge, J., Putnam, B., &Xue, M. (2016). Prediction and ensemble forecast verification of hail in the supercell storms of 20 May 2013. *Weather and Forecasting*, *31*(3), 811-825. doi:10.1175/Waf-D-15-0152.1.

Song, F. F., Feng, Z., Leung, L. R., Houze, R. A., Wang, J. Y., Hardin, J., &Homeyer, C. R. (2019). Contrasting spring and summer large-scale environments associated with mesoscale convective systems over the US Great Plains. *Journal of Climate*, *32*(20), 6749-6767. doi:10.1175/Jcli-D-18-0839.1.

Thompson, G., S. Tessendorf, A. Heymsfield, and I. Kyoko (2018), Improving graupel and hail treatment in the thompson microphysics parameterization, paper presented at North American Hail Workshop, Boulder, CO, NCAR.

Trapp, R. J., Diffenbaugh, N. S., Brooks, H. E., Baldwin, M. E., Robinson, E. D., &Pal, J. S. (2007). Changes in severe thunderstorm environment frequency during the 21st century caused by anthropogenically enhanced global radiative forcing. *Proceedings of the National Academy of Sciences of the United States of America*, *104*(50), 19719-19723. doi:10.1073/pnas.0705494104.

Trapp, R. J., &Hoogewind, K. A. (2016). The realization of extreme tornadic storm events under future anthropogenic climate change. *Journal of Climate*, *29*(14), 5251-5265. doi:10.1175/Jcli-D-15-0623.1.

Trapp, R. J., Hoogewind, K. A., &Lasher-Trapp, S. (2019). Future changes in hail occurrence in the United States determined through convection-permitting dynamical downscaling. *Journal of Climate*, *32*(17), 5493-5509. doi:10.1175/Jcli-D-18-0740.1.

Trapp, R. J., Robinson, E. D., Baldwin, M. E., Diffenbaugh, N. S., &Schwedler, B. R. J. (2011). Regional climate of hazardous convective weather through high-resolution dynamical downscaling. *Climate Dynamics*, *37*(3-4), 677-688. doi:10.1007/s00382-010-0826-y.

Varga, Á.J., Breuer, H. (2020). Sensitivity of simulated temperature, precipitation, and global radiation to different WRF configurations over the Carpathian Basin for regional climate applications. *Climate Dynamics*, *55*, 2849–2866 (2020). https://doi.org/10.1007/s00382-020-05416-x

Wang, J., Dong. X., Kennedy, A., Hagenhoff, B., Xi, B. (2019). A regime-based evaluation of southern and northern great plains warm-season precipitation events in WRF. *Weather Forecasting*, *34*, 805– 831. https://doi.org/10.1175/WAF-D-19-0025.1.

Wei, W., Li, W. H., Deng, Y., &Yang, S. (2019). Intraseasonal variation of the summer rainfall over the Southeastern United States. *Climate Dynamics*, *53*(1-2), 1171-1183. doi:10.1007/s00382-018-4345-6.

Xie, B., Zhang Q. & Wang Y. (2010). Observed Characteristics of Hail Size in Four Regions in China during 1980-2005. *Journal of Climate*. 23:4973-4982. doi: 10.1175/2010JCLI3600.1

Yang, Q., Houze, R. A., Leung, L. R., &Feng, Z. (2017). Environments of long-lived mesoscale convective systems over the central United States in convection permitting climate simulations. *Journal of Geophysical Research-Atmospheres*, *122*(24), 13288-13307. doi:10.1002/2017jd027033.

Zhou, Z. W., Zhang, Q. H., Allen, J. T., Ni, X., &Ng, C. P. (2021). How many types of severe hailstorm environments are there globally? *Geophysical Research Letters*, *48*(23). doi:10.1029/2021GL095485.

Ziegler, C. L., Ray, P. S., &Knight, N. C. (1983). Hail growth in an Oklahoma multicell storm. *Journal of the Atmospheric Sciences*, *40*(7), 1768-1791. doi:10.1175/1520-0469(1983)040<1768:Hgiaom>2.0.Co;2.

Table 1 The list of storm cases and their major storm periods. The region is also shown as a black box in Fig. 1.

Type	Case	Major storm period	Time	Region
Frontal systems	Case 1	1900 UTC 18 April 2015 - 0830 UTC 19 April 2015	1600 UTC 18 April 2015	Lat: 30.5,34.5 Lon: -101.7, -98.5
	Case 2	2300 UTC 1 April 2015 - 0830 UTC 2 April 2015	1800 UTC 1 April 2015	Lat: 38.5,40.7 Lon: -104.1, -101.8
	Case 3	1900 UTC 19 April 2015 - 0300 UTC 20 April 2015	1600 UTC 19 April 2015	Lat: 29.8,33.3 Lon: -96.6, -93.0
	Case 4	1800 UTC 10 May 2016 – 0800 UTC 11 May 2016	1600 UTC 10 May 2016	Lat: 37.0,39.8 Lon: -104.9, -101.8
GPLLJs	Case 5	1600 UTC 25 May 2015 – 0430 UTC 26 May 2015	1500 UTC 25 May 2015	Lat: 30.5,35.1 Lon: -102.6, -98.1
	Case 6	1700 UTC 26 May 2015 – 0430 UTC 27 May 2015	1500 UTC 26 May 2015	Lat: 30.4,33.5 Lon: -102.0, -98.7
	Case 7	1800 UTC 10 April 2017 - 0500 UTC 11 April 2017	1500 UTC 10 April 2017	Lat: 28.0,32.8 Lon: -100.5, -95.7
	Case 8	1800 UTC 16 May 2017 – 0200 UTC 17 May 2017	1500 UTC 16 May 2017	Lat: 29.8,34.2 Lon: -104.1, -100.0

Figure 1 Large-scale environmental variables in the current climate. (a) wind speed (shading) and geopotential height (contour) at 500 hPa (left) and specific humidity (shading) and winds (arrow) at 850 hPa (right) for four frontal cases. (b) Same as (a), except for four GPLLJ cases. The data is from the RAP analysis. The black boxes denote the regions for the pre-convection meteorological analysis shown in Figure 2. The latitudes and longitudes of the black box regions are shown in Table 1.

Figure 2 Frequency distributions of the pre-convection meteorological variables in current and future climate. (a) Temperature (2-m), precipitable water, CAPE, CIN, wind shear (0-6 km), and SRH (0-3 km) for current (black) and future (red) frontal storms. (b) Same as (a), except for the GPLLJs. The numbers shown on each panel are the mean values. The data are from the WRF model simulations over the region where the storm is initiated at the time prior to the convection. The region and time for each case are shown in Table 1. Note the region for each case crosses a few hundred kilometers and is shown as a black box in the left panels of Figure 1. Similar results are obtained when expanding or shrinking the selected box size.

Figure 3 Evaluation of the storm properties in the current climate. Frequency distributions of (a) composite (column maximum) radar reflectivity, (b) precipitation rate, and (c) hail in the frontal systems (left) and the GPLLJs (right). The observation and simulation are shown as grey and black bars, respectively. The observations are from the Next Generation Weather Radar (NEXRAD) system, Stage IV, and MESH for radar reflectivity, precipitation rate, and hail, respectively. The analyses are for the major storm periods of the tracked storms.

Figure 4 Occurrences of hail and precipitation on the surface for the current and future hailstorms and their relative changes from the current to future hailstorms. (a) Occurrences of different hail categories: non-severe (0.5 cm $\leq$ diameter $<$ 2.5 cm), severe (2.5 cm $\leq$ diameter $<$ 5.1 cm), and significant severe hail (5.1 cm or larger) in the current (grey or black) and the future (red) hailstorms and (b) the relative changes (%) from the current to future climate. (c and d) Same as (a and b) except for the occurrences of different precipitation categories: weak (0.1 mm h^{-1} $<$ rain rate $\leq$ 5 mm h^{-1}), moderate (5 mm h^{-1} $<$ rain rate $\leq$ 20 mm h^{-1}), and heavy ($>$ 20 mm h^{-1}). (e and f) same as (c, d), except for the total precipitation of each precipitation category. The hailstorms are tracked and analyzed over the major storm periods, which vary by case as shown in Table 1.

Figure 5 Profiles of updraft velocity, updraft width, graupel mass mixing ratio, hail mass mixing ratio, and the mean bulk hail size in the current (black) and future (red) climate for (a) frontal storms and (b) GPLLJ storms. The analysis is for grids with $w > 5$ m s^{-1}. The updraft width at each level is represented by the number of horizontally adjacent updraft grids with $w > 5$ m s^{-}. The line shows the mean values of all four cases for each storm type and the shaded area shows the standard deviation. The percentage changes from the current to future climate are shown as dashed lines with the secondary x-axis. The mean melting-level height is shown as dashed black

and red lines for the current and future climate, respectively. Note the hail peaks at the level much higher than the melting level because the results are for the strong updrafts with $w > 5$ m s^{-1}. The hail peak level is near the melting level when the updraft threshold is changed to 0 m s^{-1}.

Figure 6 Same as Figure 5, except for cloud water mass mixing ratio, rainwater mass mixing ratio, cloud water mass flux, and rainwater mass flux from left to right.

Figure 7 Same as Figure 5, except for vertical velocity components. From the left to right, they are the vertical pressure perturbation gradient (PPG) force, thermal buoyancy, hydrometeor loading effect, and entrainment (represented by the residual of the ratio of liquid water content to the adiabatic liquid water content). The hydrometeor loading effect is represented with the negative sign thus more negative means a larger effect.

Figure 8 Frequency distribution of warm cloud depth in the convective cores from (a) the frontal systems, (b) the GPLLJs, and (c) the change of warm cloud depth from the current to future hailstorms for both systems. (d, e, f) The same as (a, b, c), except for the melting-level height. (g, h, i) the same as (a, b, c), except for cloud base height. Black and red are for the current and future simulations, respectively. The convective cores of the storm are identified with the criteria: (1) the cloud base is below the melting-level height and the cloud thickness is larger than 5 km and (2) the depth of updraft velocity of > 2 m s^{-1} is at least 4 km. The numbers shown on the left and middle panels are the mean values.

Figure 9 Schematic depiction of the responses of the hailstorms to anthropogenic climate change (ACC). Occurrences of large hail notably increase from the current (top) to the future climate (bottom) in the frontal systems (left), mainly due to the enhanced convective intensity and updraft width (purple arrow). Whereas the occurrences of large hail for the GPLLJ storms (right) are not sensitive to ACC because of a very small change in the convective intensity and width and a larger increase in the warm cloud depth (WCD) compared with the frontal storms.

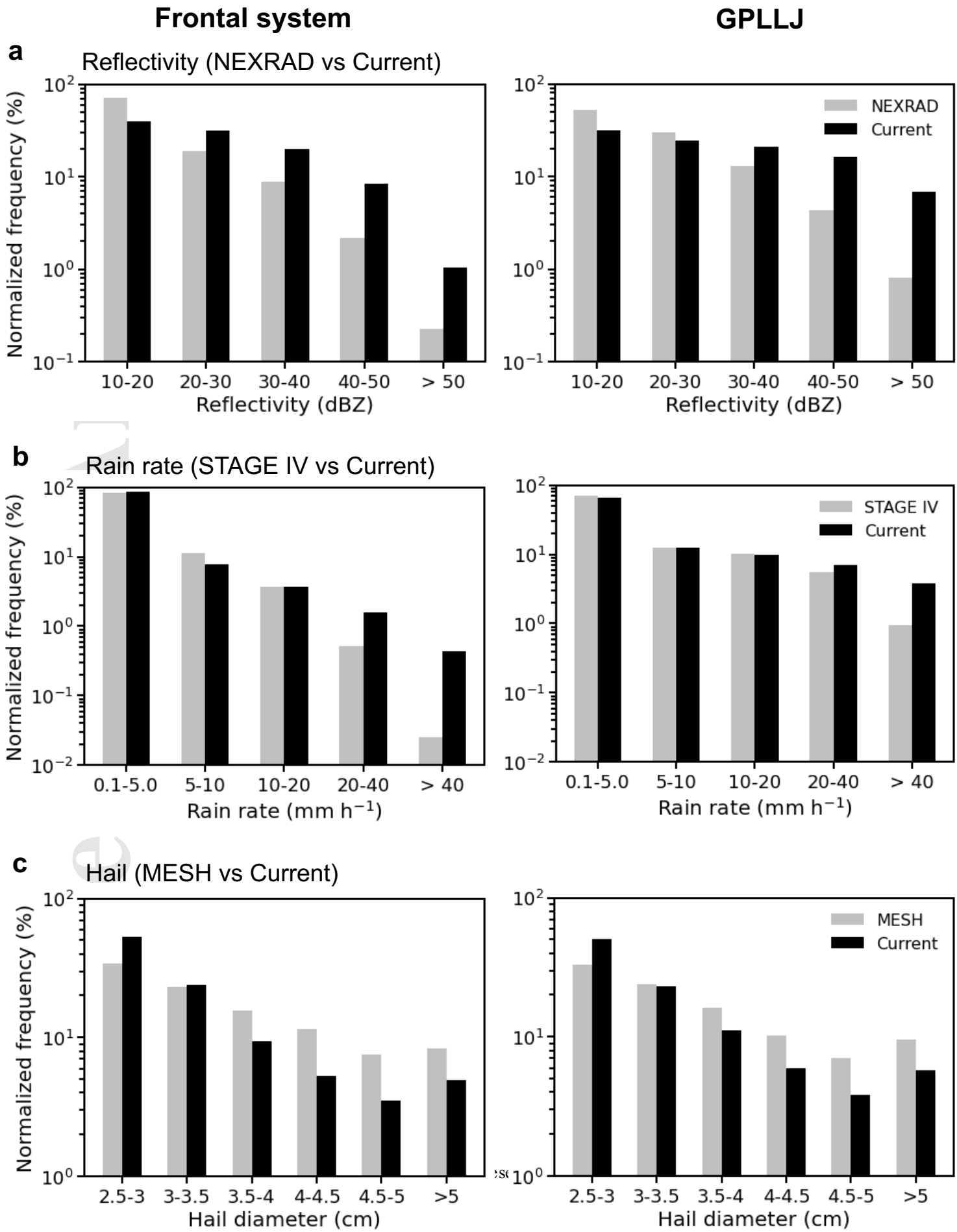
Frontal system
GPLLJ
a
Reflectivity (NEXRAD vs Current)
Normalized frequency (%)
NEXRAD
Current
10-20
20-30
30-40
40-50
> 50
Reflectivity (dBZ)
b
Rain rate (STAGE IV vs Current)
STAGE IV
0.1-5.0
5-10
10-20
20-40
> 40
Rain rate (mm h^{-1})
c
Hail (MESH vs Current)
MESH
2.5-3
3-3.5
3.5-4
4-4.5
4.5-5
>5
Hail diameter (cm)

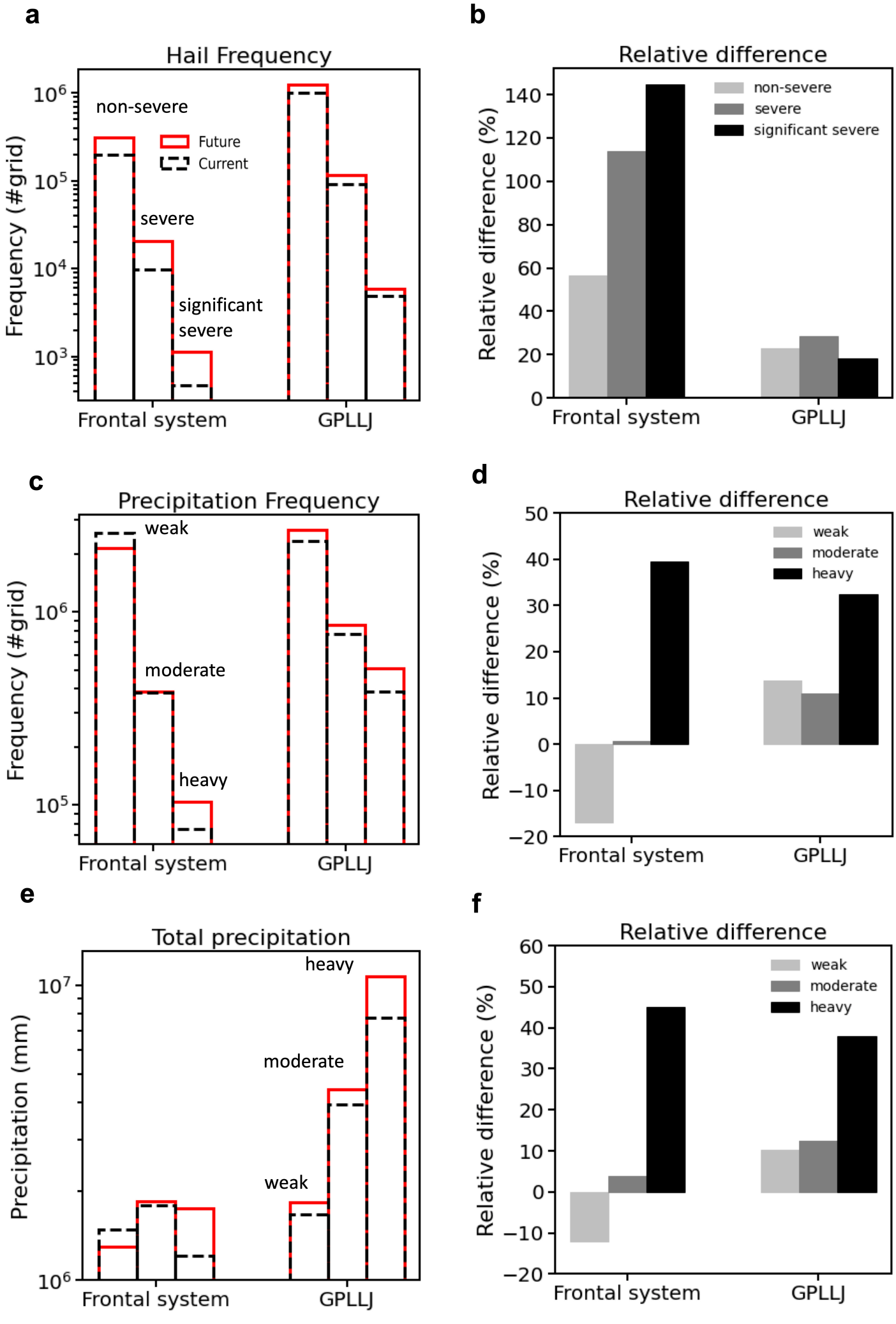
a
Hail Frequency
Frequency (#grid)
non-severe
Future
Current
severe
significant severe
Frontal system
GPLLJ
b
Relative difference
Relative difference (%)
non-severe
severe
significant severe
Frontal system
GPLLJ
c
Precipitation Frequency
Frequency (#grid)
weak
moderate
heavy
Frontal system
GPLLJ
d
Relative difference
Relative difference (%)
weak
moderate
heavy
Frontal system
GPLLJ
e
Total precipitation
Precipitation (mm)
heavy
moderate
weak
Frontal system
GPLLJ
f
Relative difference
Relative difference (%)
weak
moderate
heavy
Frontal system
GPLLJ

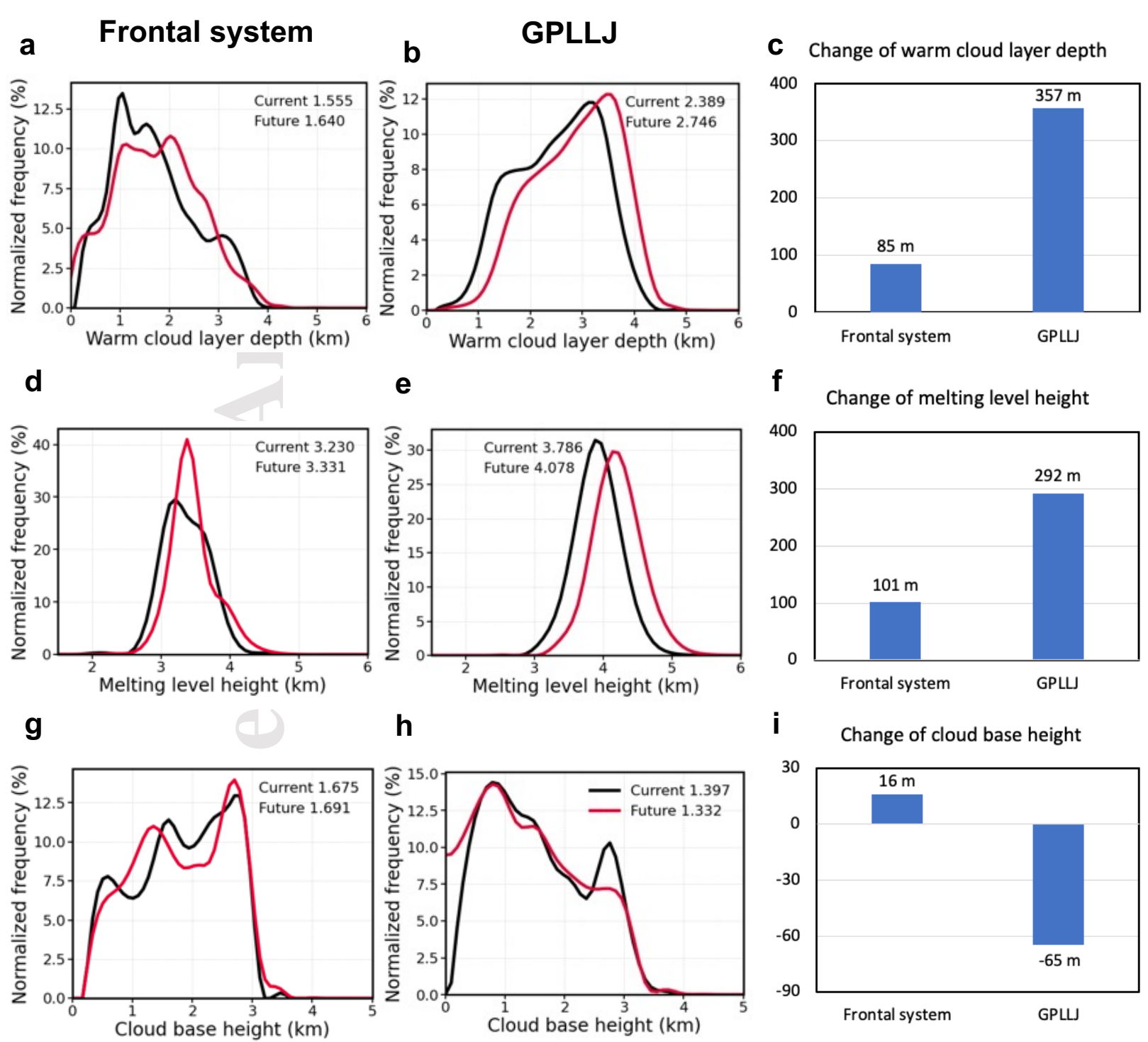
Frontal system
GPLLJ
a
b
c
Change of warm cloud layer depth
Normalized frequency (%)
Current 1.555
Future 1.640
Warm cloud layer depth (km)
Current 2.389
Future 2.746
Warm cloud layer depth (km)
357 m
85 m
Frontal system
GPLLJ
d
e
f
Change of melting level height
Current 3.230
Future 3.331
Melting level height (km)
Current 3.786
Future 4.078
Melting level height (km)
292 m
101 m
Frontal system
GPLLJ
g
h
i
Change of cloud base height
Current 1.675
Future 1.691
Cloud base height (km)
Current 1.397
Future 1.332
Cloud base height (km)
16 m
-65 m
Frontal system
GPLLJ

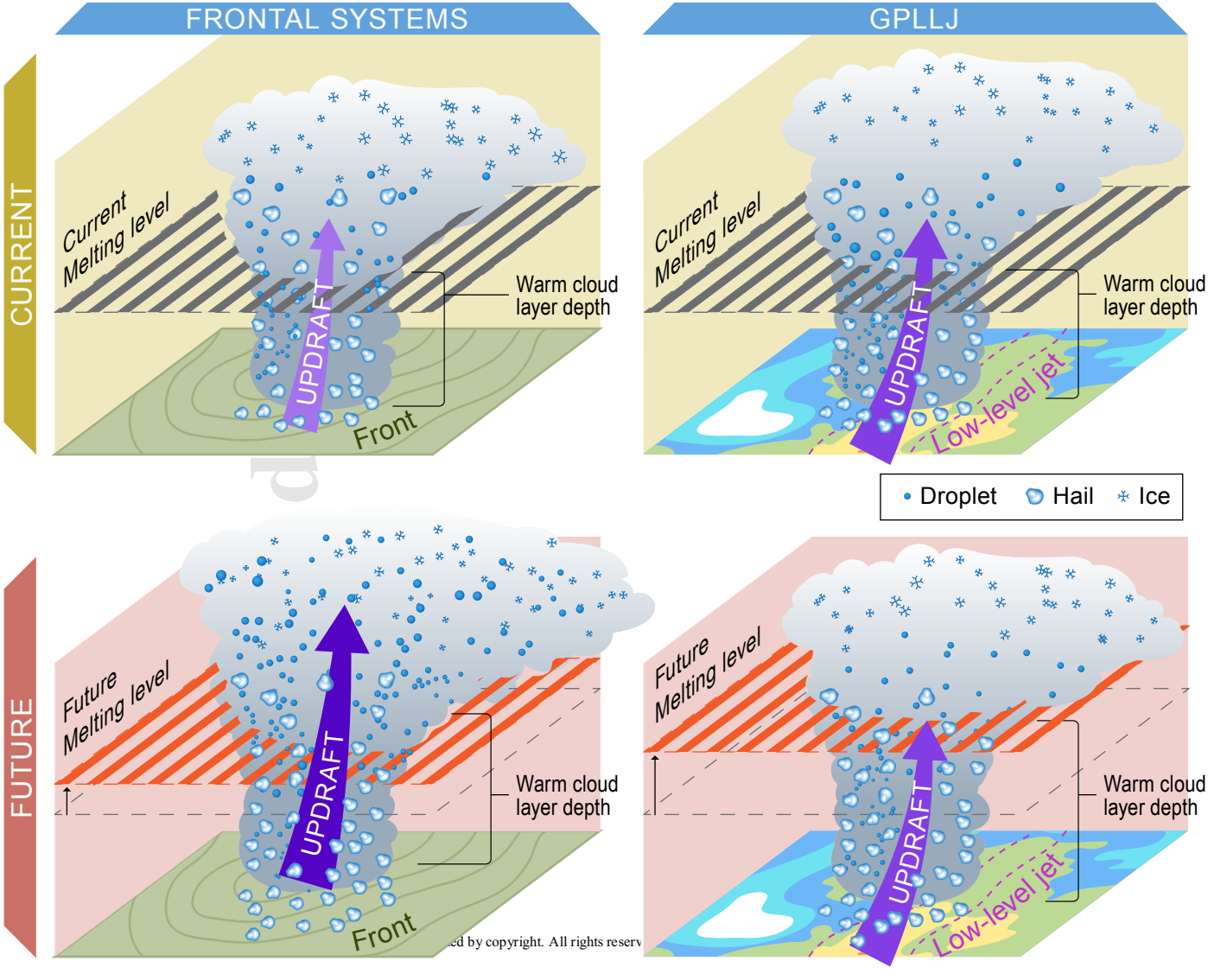

a. Frontal system

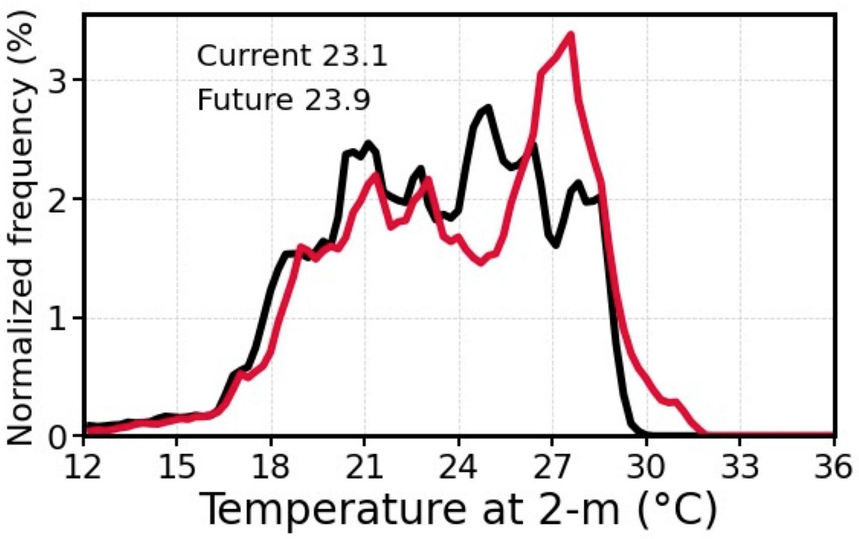

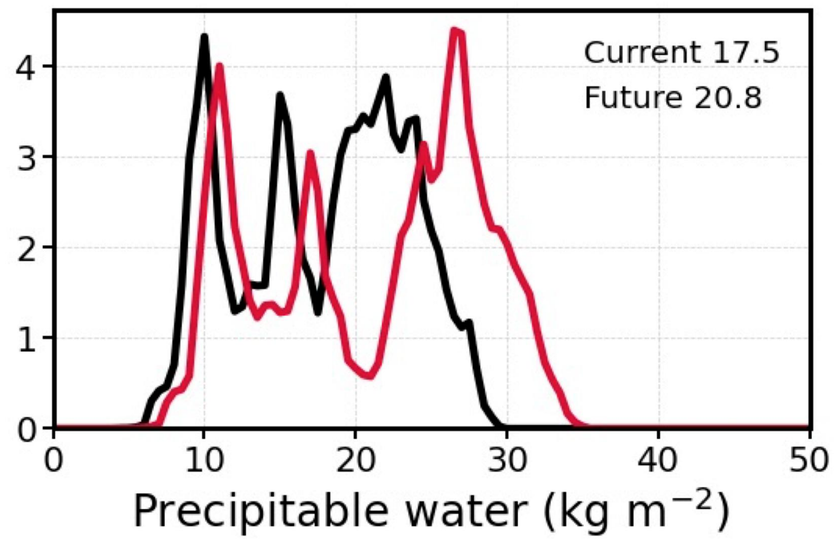

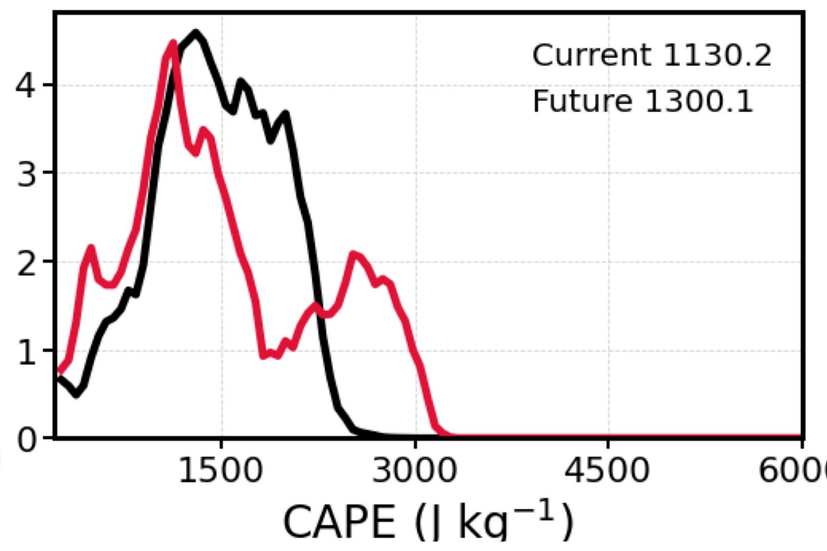

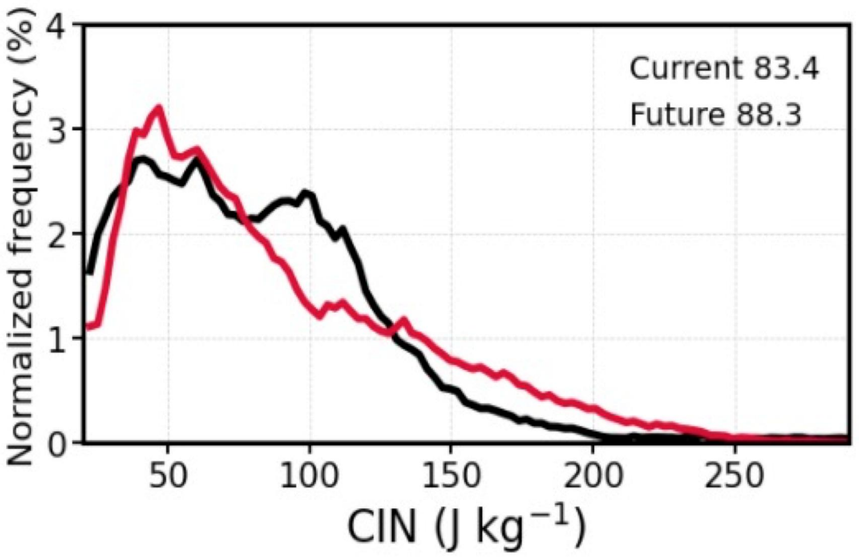

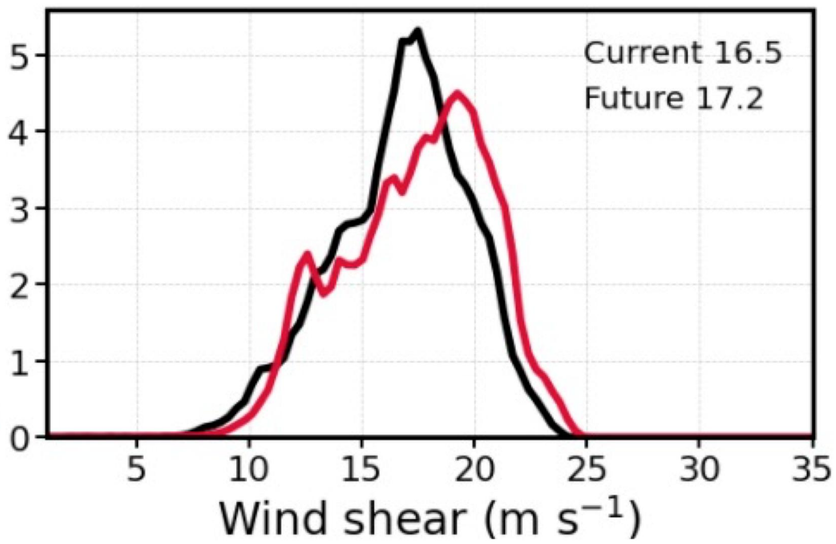

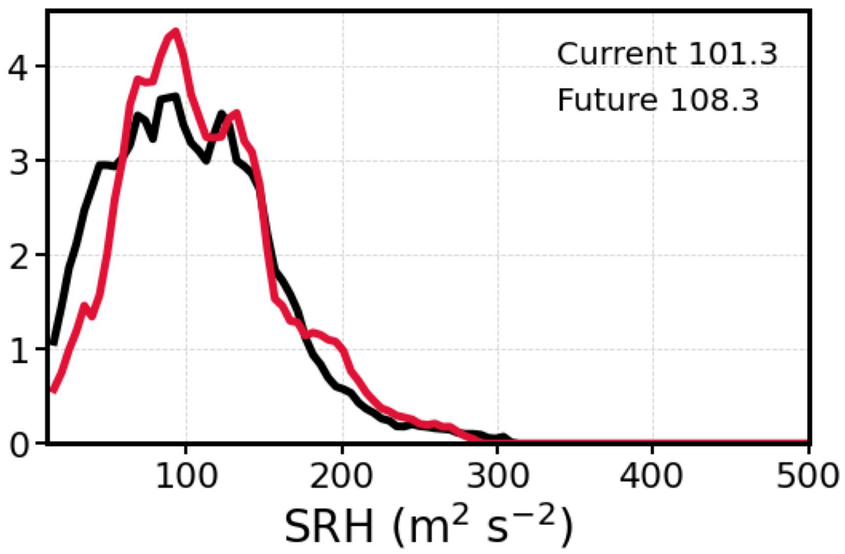

b. GPLLJ

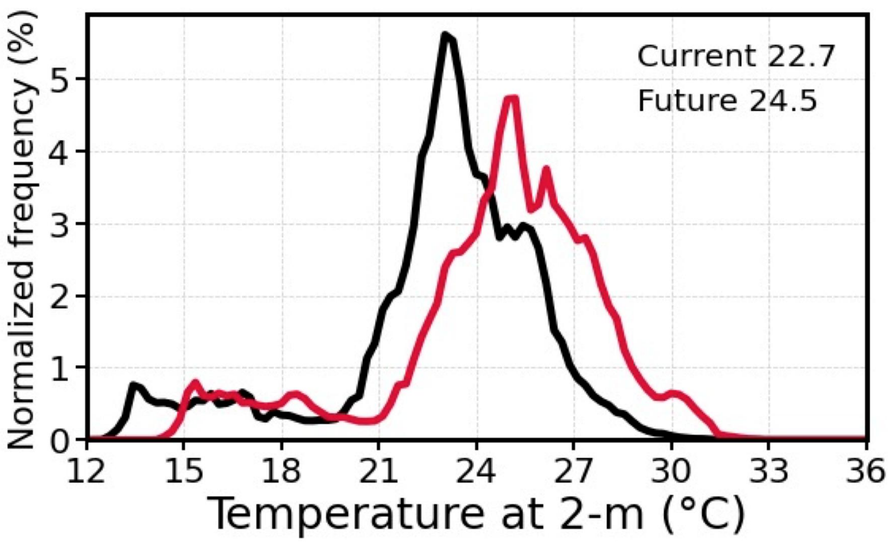

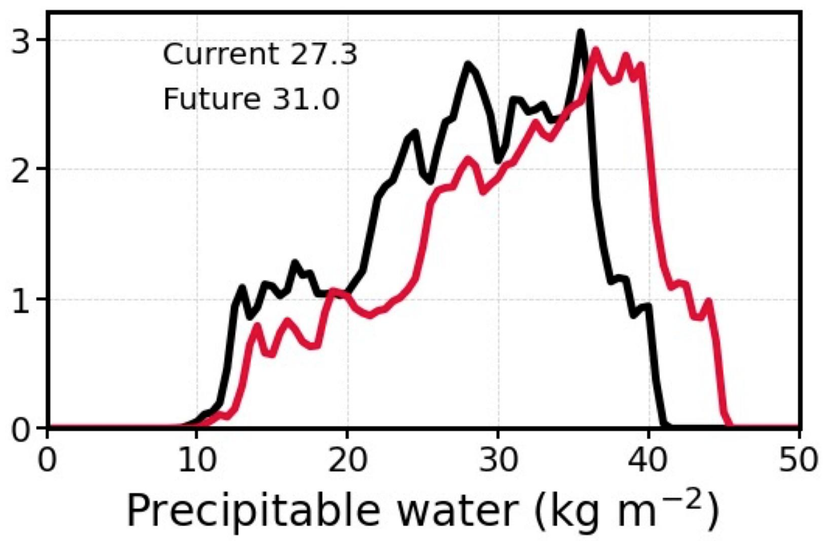

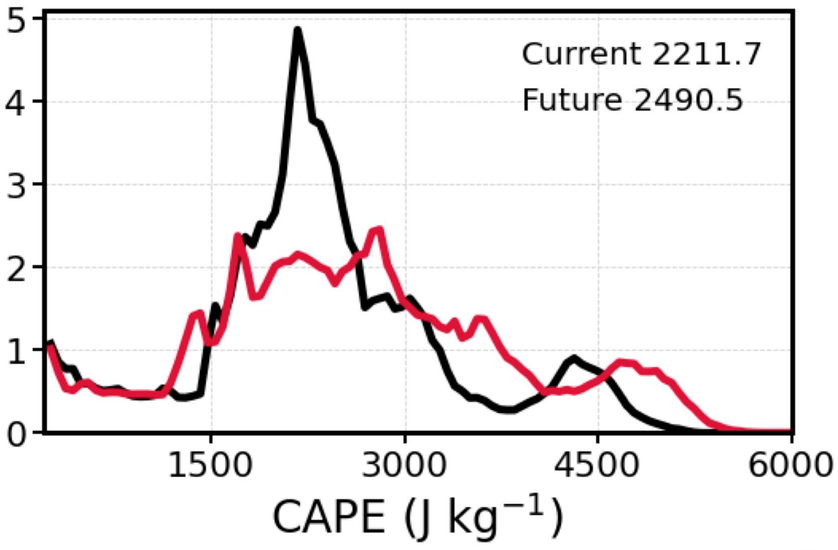

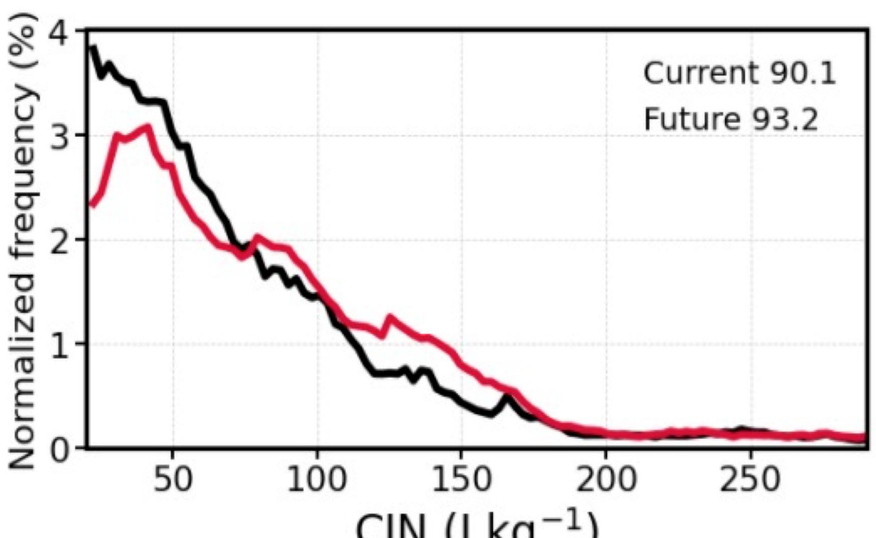

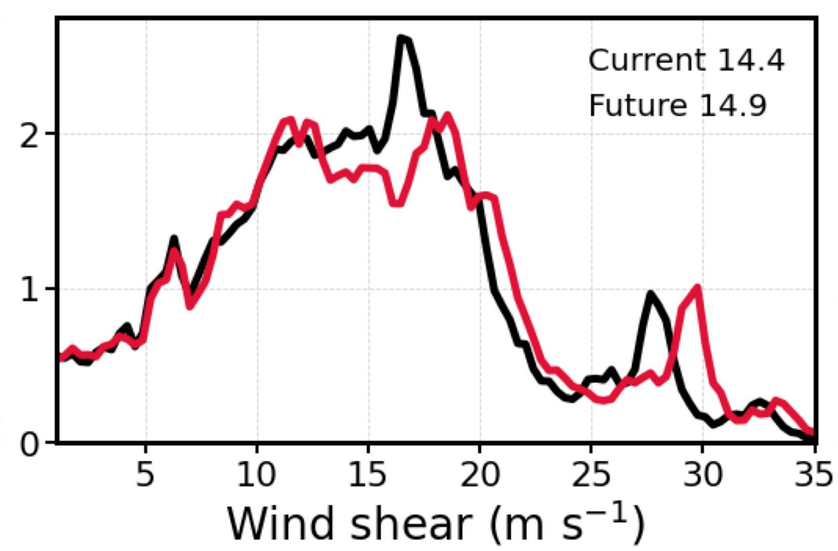

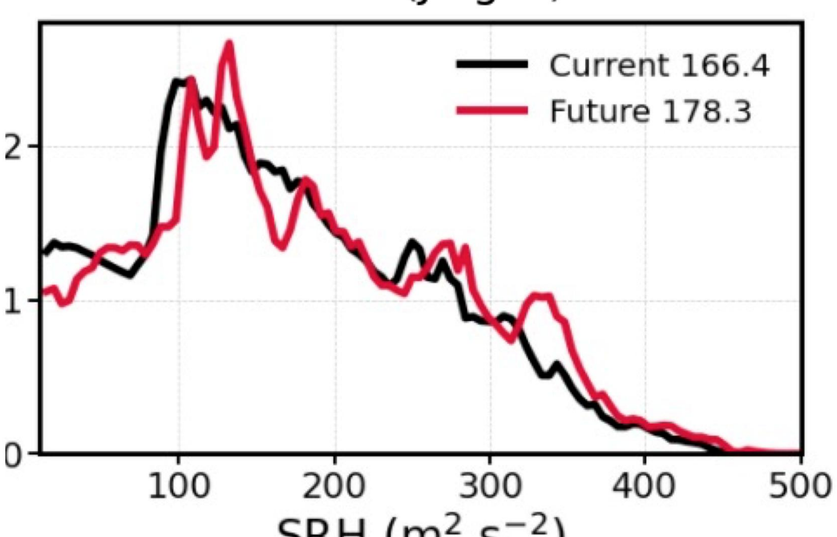

a. Frontal system

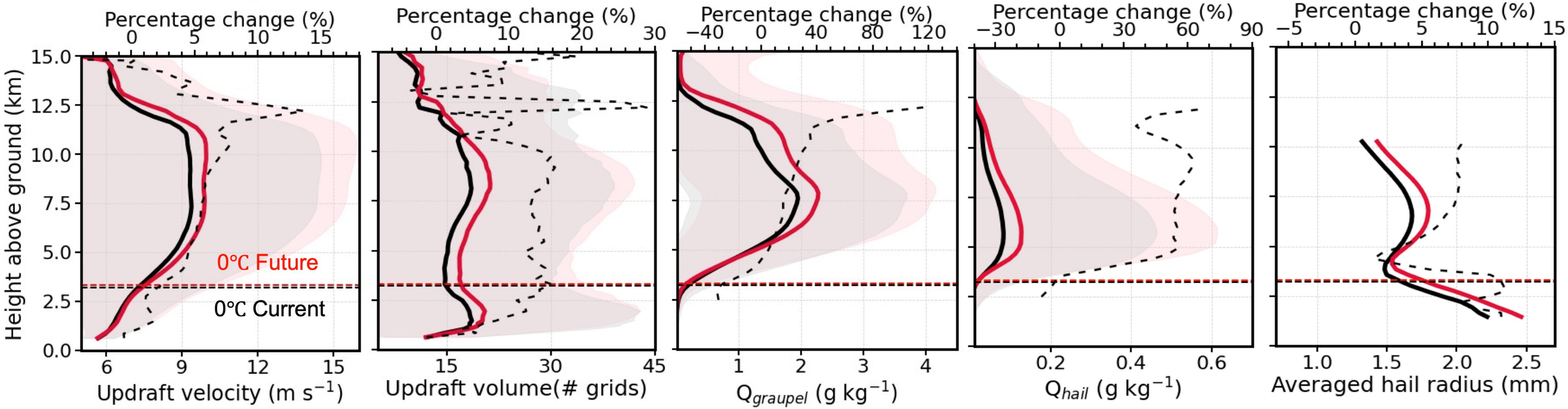

b. GPLLJ

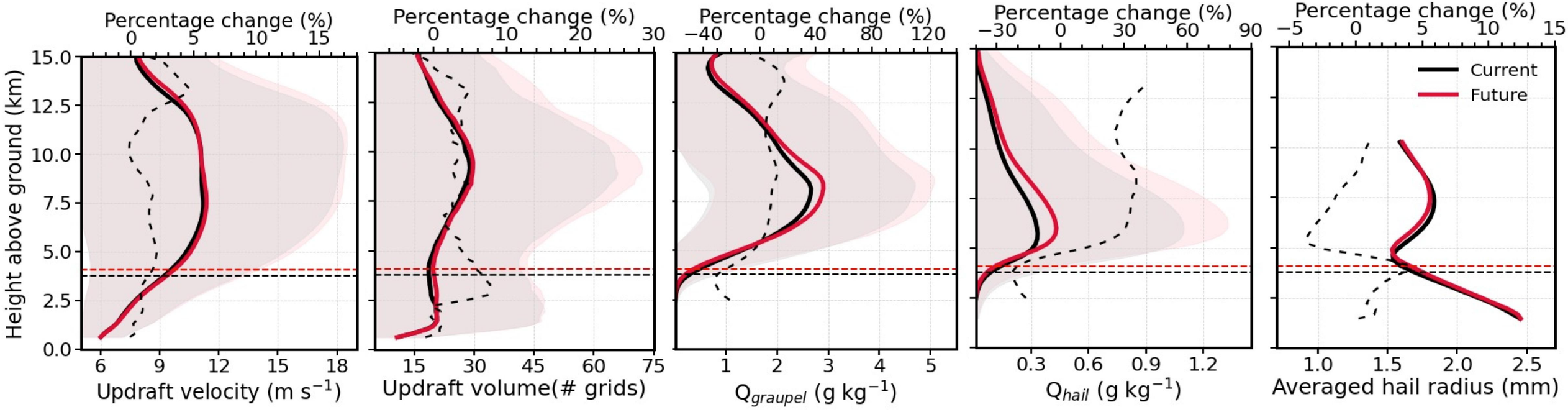

a. Frontal system

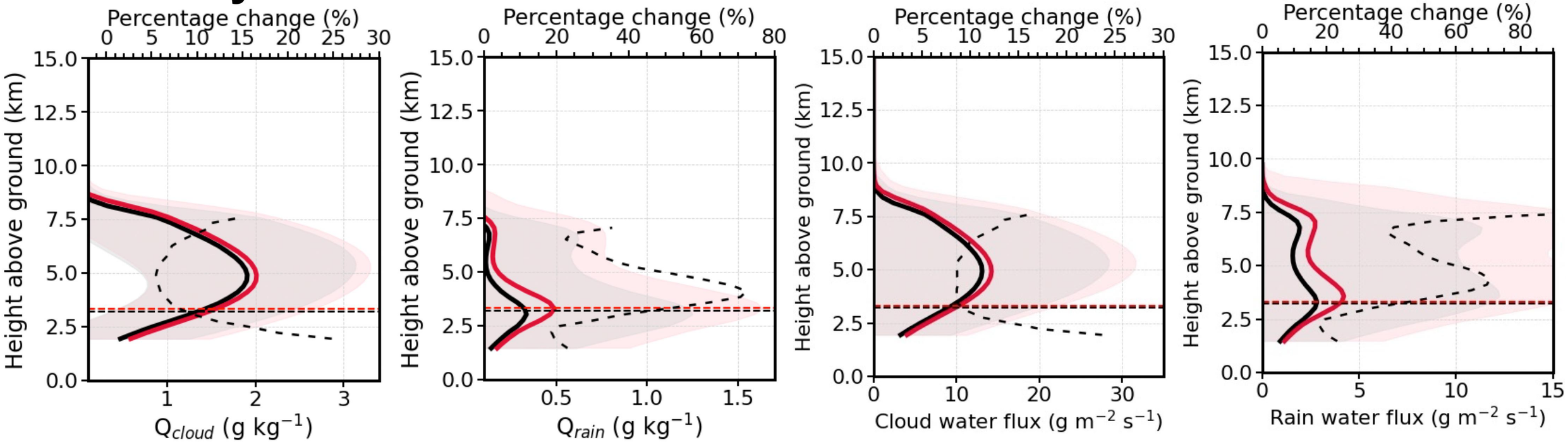

b. GPLLJ

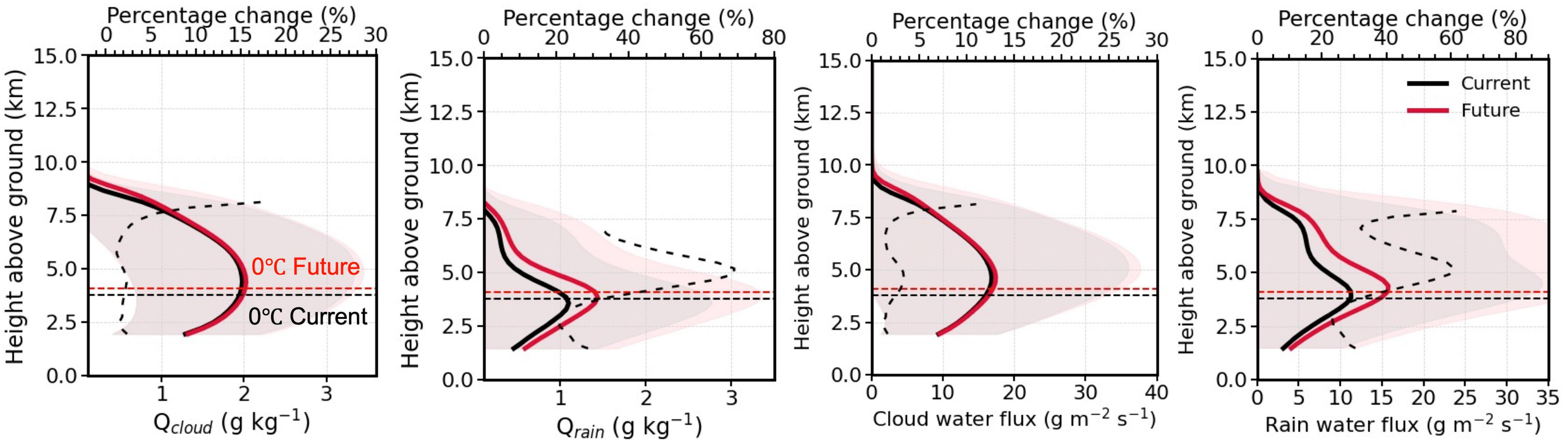

a. Frontal system

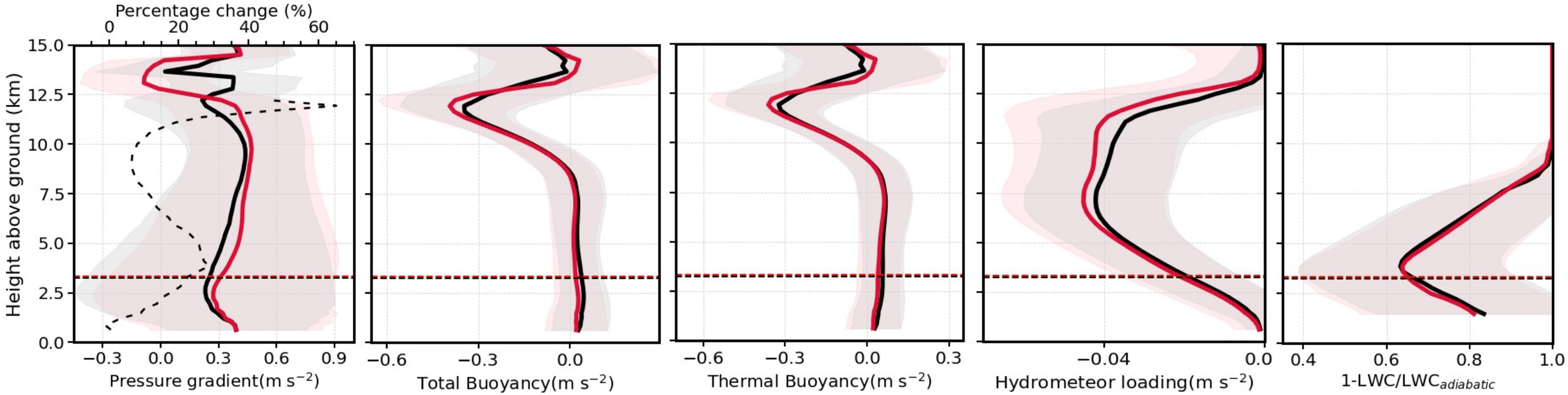

b. GPLLJ

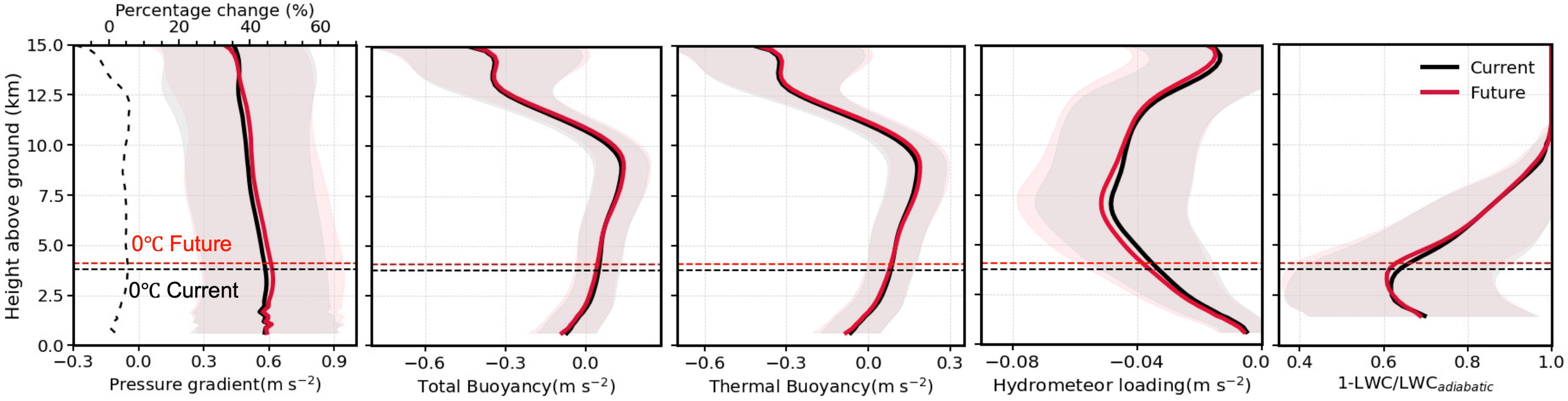

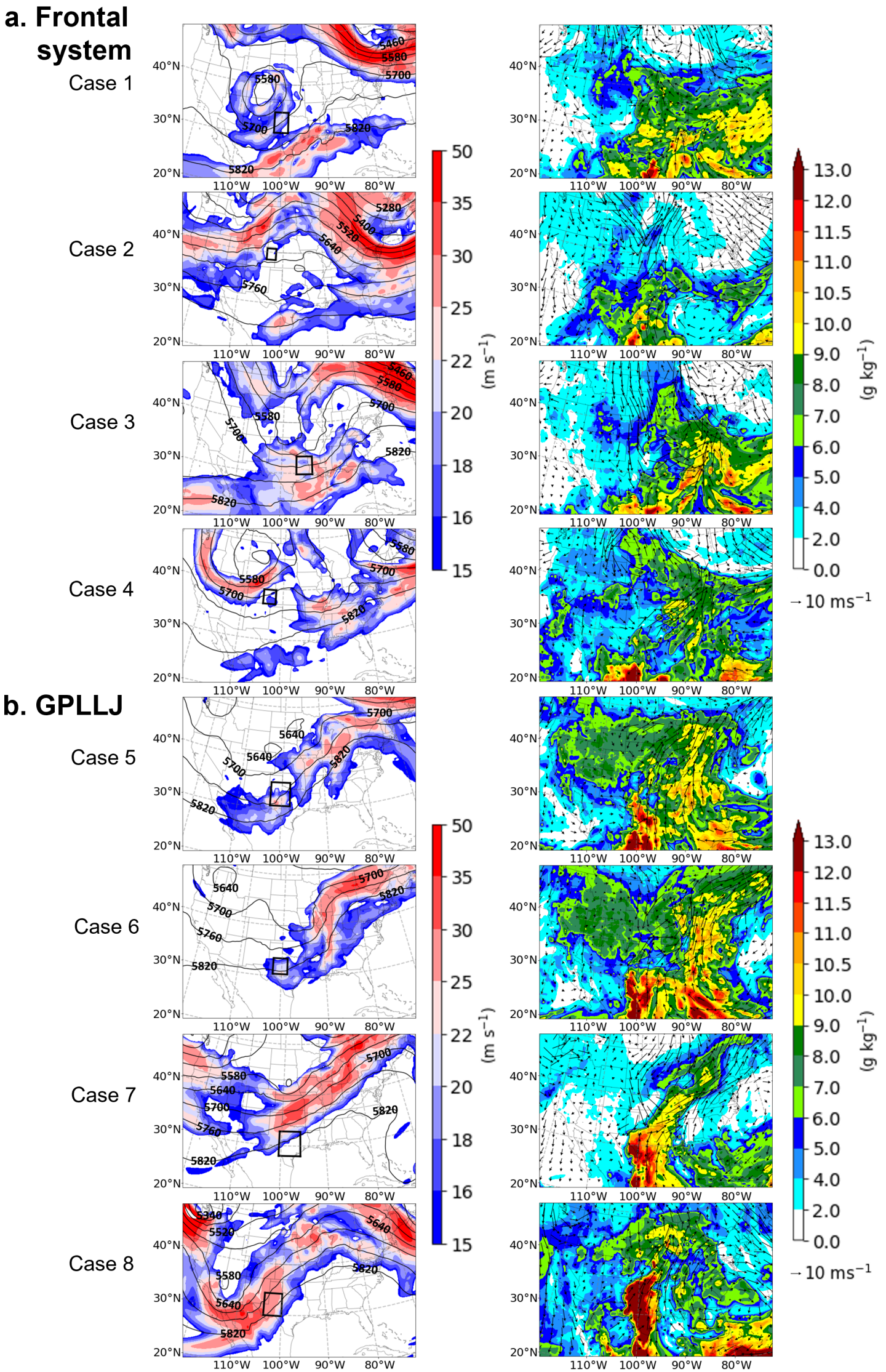
a. Frontal system
Case 1
Case 2
Case 3
Case 4
b. GPLLJ
Case 5
Case 6
Case 7
Case 8
40°N
30°N
20°N
110°W
100°W
90°W
80°W
5460
5580
5700
5820
5280
5400
5520
5640
5760
5340
50
35
30
25
22
20
18
16
15
(m s^{-1})
13.0
12.0
11.5
11.0
10.5
10.0
9.0
8.0
7.0
6.0
5.0
4.0
2.0
0.0
(g kg^{-1})
→ 10 ms^{-1}